Acceleration of Late Pleistocene Activity of a Central European Fault Driven by Ice Loading

Petra Štěpančíková [1)*], Thomas K. Rockwell [1,2)], Jakub Stemberk [1)], Edward J. Rhodes [3,4)], Filip Hartvich [1)], Karen Luttrell [5)], Madeline Myers [5,6)], Petr Tábořík [1)], Dylan H. Rood [7)], Neta Wechsler [8)], Daniel Nývlt [9)], María Ortuño [10)], Jozef Hók [11)]

[1)] Inst. of Rock Structure and Mechanics, Czech Acad. of Sci., Prague, Czech Rep.
[2)] Dept. of Geol. Sci., San Diego State Univ., California
[3)] Dept. of Geography, Univ. of Sheffield, S10 2TN UK
[4)] Dept. of Earth, Planetary and Space and Sciences, University of California Los Angeles, CA, USA
[5)] Dept. of Geology and Geophysics, Louisiana State Univ., Baton Rouge, Louisiana
[6)] Dept. of Geography and Planning, Queen's University, Kingston, Ontario, Canada
[7)] Dept. of Earth Science and Engineering, Royal School of Mines, Imperial College London, UK
[8)] Neev Center for Geoinformatics, Fredy & Nadine Herrmann Institute of Earth Sciences, The Hebrew University of Jerusalem, Israel
[9)]Faculty of Science, Masaryk Univ., Brno, Czech Rep.
[10)] Risknat-Institute Geomodels, Dept. of Earth and Ocean Dynamics, University of Barcelona, Spain
[11)] Faculty of Science, Comenius Univ., Bratislava, Slovakia

**corresponding author, stepancikova@irsm.cas.cz, Institute of Rock Structure and Mechanics, Czech Academy of Sciences, V Holešovičkách 41, Prague 8, 18209, Czech Republic*

Abstract

We studied the southern part of the NW-SE trending Sudetic Marginal fault (SMF), situated at the northeastern limit of the Bohemian Massif in central Europe, to assess its Quaternary activity. Eighteen trenches and thirty-four electric resistivity profiles were performed at Bílá Voda to study the fault zone and 3-dimensional distribution of a beheaded alluvial fan on the NE side of the fault. We interpret a small drainage, located about 29-45 m to the SE of the fan apex, as the only plausible source channel implying a similar amount of left-lateral offset. The alluvial fan deposits radiometric ages range between about 24 and 63 ka, but postglacial deposits younger than 11 ka are not displaced, indicating that all motion occurred in the late Pleistocene. The site lies ~150 km south of the late Pleistocene Weichselian maximum (~20 ka) ice sheet front. We model the effects of the ice load on lithospheric flexure and resolved fault stresses, and show that slip on the SMF was promoted by the presence of the ice sheet, resulting in a late Pleistocene slip rate of ~$1.1^{+2.3}/_{-0.6}$ mm/yr. As the most favorable time for glacial loading-induced slip would be during the glacial maximum between about 24 and 12 ka, it is doubtful that the slip rate remained constant during the entire period of activity, and if most slip occurred during this period, the short-term rate may have been even higher. Considering that the modern maximum principal stress (σ_1) is oriented nearly parallel to the Sudetic Marginal fault (NNW-SSE) and is thus unfavorable for fault motion, our observations suggest that the likelihood of continued motion and earthquake production is much lower in the absence of an ice sheet.

Keywords: paleoseismology, intraplate earthquakes, ice-loading, glacially triggered fault, Sudetic Marginal fault, Central Europe

1. Introduction

Identification of active faults is important to correctly assess seismic hazard to societies. Intraplate Europe is generally known as a region of low seismicity. Nevertheless, there are several cases where Late Quaternary faulting has been identified in central European Variscan orogenic belt (see cf. Štěpančíková et al., 2019; Hürtgen et al., 2021 and references therein; Steffen et al., 2021 and references therein).

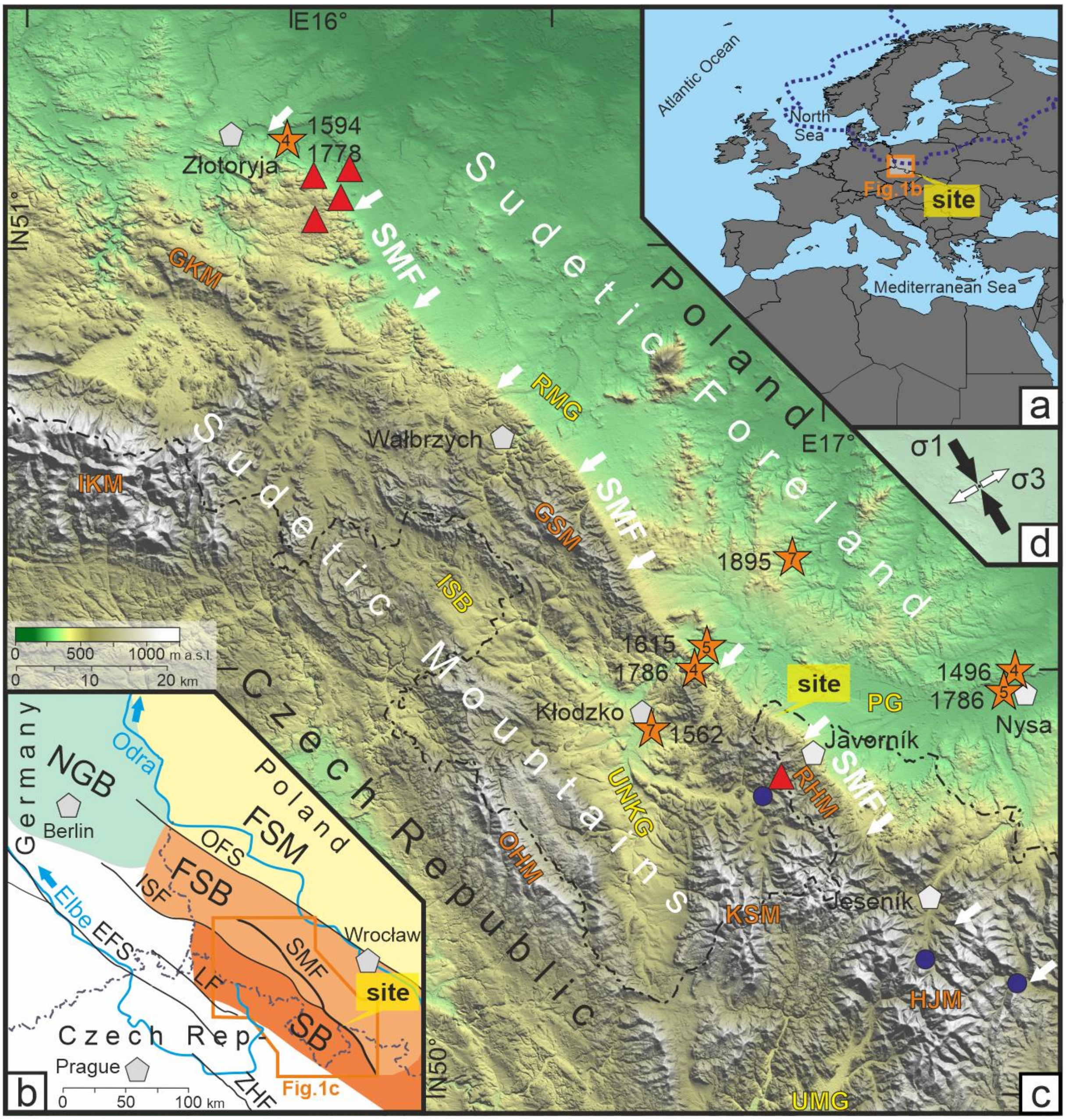

Fig. 1 a) Site localization on the Europe map. Blue dotted line shows LGM ice sheet extent (Ehlers et al. 2011); b) Simplified tectonic map modified after Scheck et al. (2002). Main faults and fault zones:

EFS – Elbe fault system zone, ISF – Intra-Sudetic main fault, LF – Lužický fault, OFS – Odra fault zone, SMF – Sudetic Marginal fault, ZHF – Železné hory fault; Main geological units: BM – Bohemian Massif that includes also FSB and SB, FSB – Fore-Sudetic block, FSM – Fore-Sudetic Monocline, NGB – North German basin, SB – Sudetic block; c) Relief map of the Sudetes using SRTM (resolution 30m; Farr (Eds.), 2007). Orange stars: epicenters of historical earthquakes with intensity (I_0) and year; Rectangles: Tertiary volcanoes; Blue dots – thermal and mineral springs; Basins: ISB – Intra-Sudetic Basin, PG – Paczków Graben, RMG – Roztoki–Mokrzeszow graben, UMG – Upper Moravia Graben, UNKG – Upper Nysa Kłodzka Graben. Mountains: GKM – Góry Kaczawskie Mts., GSM – Góry Sowie Mts., HJM – Hrubý Jeseník Mts., OHM – Orlické hory Mts., IKM – Izera - Krkonoše Mts., KSM – Kralický Sněžník Mts., RHM – Rychlebské hory Mts./Góry Złote Mts; d) current stress field from focal mechanism adopted from Špaček et al. (2006).

The activity of seismogenic faults, while mostly driven by far-field plate tectonics forces, can also be affected by near-field changes in the crustal stresses, which may either promote or inhibit seismic activity. Sources of significant stress change can result from activity on near-by faults (King et al., 1994), which predominates over one or several seismic cycles, and vertical load changes caused by climate driven mass fluctuations, which include volumetric variations in ocean basins, ice caps, glaciers and lakes and associated erosion-deposition processes (Stewart et al., 2000; Luttrell et al., 2007; Luttrell and Sandwell, 2010; Hampel et al., 2010) that act over longer time scales. Related fluid pressure effects also play a part in changing seismicity patterns and earthquake nucleation processes (Byerlee, 1993). Moreover, it was demonstrated that seismic activity can ensue after deglaciation in otherwise seismically quiescent continental shields and cause faulting in previously inactive areas, such as northern and central Europe, with an increasing number of such studies where fault activity has been ascribed to glacially induced loading; some with postglacial slip and increased deglaciation seismicity (Arvidsson, 1996; Houtgast et al., 2005; Stewart et al., 2000; Turpeinen et al., 2008;

Brandes et al., 2015; Steffen et al., 2021 and references therein). The effect of mass loading and unloading on crustal deformation can extend to several hundred kilometers beyond the limits of the loading mass (James and Bent, 1994).

We present here the results of a field paleoseismic study (Bílá Voda site) where geological and geophysical data show that the Sudetic Marginal fault bounding the northeastern Bohemian Massif (Czech Republic) in central Europe sustained major displacement in latest Pleistocene time with a relatively fast slip rate with respect to its intraplate position, yet no significant displacement in the Holocene (Fig. 1). As the SMF is located in the area of the former forebulge of the Fennoscandian ice sheet and the Bílá Voda study site (located at the border of Czech Republic with Poland) lies about 150-170 km south from the late Pleistocene Weichselian (~20 ka) ice front (Ehlers et al., 2011), we applied modeling to test the hypothesis of causal relationship between fault acceleration and ice loading. The modeling demonstrates that the presence of the northern European ice-sheet during the last glacial maximum caused sufficient stress perturbations to promote fault motion, followed by at least 11 thousand years of inactivity after removal of the ice as also evidenced by geological data.

2. Geological setting

The Sudetic Marginal fault (SMF) is a major NW striking and NE-steeply dipping structure situated at the northeastern limit of the Bohemian Massif in central Europe, extending through Poland and Czech Republic. It exhibits a pronounced 140 km-long morphological escarpment (Fig. 1). The fault divides the elevated Sudetic Mountains block of Proterozoic to Paleozoic crystalline bedrock from the gently undulated Sudetic Foreland block, comprising deeply eroded crystalline basement, Neogene basins, and volcanics. SMF is a part of the regional-scale WNW-striking Elbe Fault System, which has had variable kinematics since the Late Carboniferous Variscan orogeny (Scheck et al., 2002). The fault likely initiated with a predominantly dextral sense of slip (Oberc, 1991) but then acted as a normal fault during a period of early Late Cretaceous basin formation. The sense of slip was reversed in the Late Cretaceous (Danišík et al., 2012) during transpressional deformation induced by far-field stress from Europe-Iberia-Africa convergence, which resulted in basin inversion in much of central Europe (Scheck et al., 2002; Kley and Voigt, 2008). The fault was reactivated in the Miocene as a transtensional oblique-slip structure that cuts Oligocene intrusions (Birkenmajer et al., 1977), and its normal component of motion resulted in the accumulation of 300-600 m of fluvial and lacustrine sediments in several sub-basins in northeastern Czech Republic and southwestern Poland (e.g. Badura et al., 2004). The uplift of the footwall of the SMF, which is responsible for the current mountainous topography, is considered to have started in Miocene/Pliocene time (Krzyszkowski et al., 2000).

Evidence for Quaternary reactivation of the SMF is found in the geomorphology of the landscape along the fault, including a relatively linear 140 km-long mountain front that expresses triangular or trapezoidal facets, hanging wine-glass valleys and deep incision of the Sudetic Mountains with consequent deposition of alluvial fans along the range margin (Fig. 1; Badura et al., 2007; Krzyszkowski and Pijet, 1993). Along the Polish portion of the fault, middle Pleistocene fluvial terraces are truncated by the SMF and show scarp heights of 15-25 m, whereas Late Pleistocene terraces have scarp heights of 10-15 m (Krzyszkowski et al., 2000).

The SMF-controlled mountain front also represented a significant barrier for the Pleistocene ice sheet, which reached the Sudetes during mid-Pleistocene Elsterian (MIS 12) and Saalian (MIS 10-6) glaciations, and which penetrated into valleys and several intramontane basins. During the late Pleistocene Weichselian glaciation (MIS 4-2), which had at least two major advances of the ice sheet in Poland ((60-50 ka), and LGM (24-19 ka)), the Bílá Voda study site lies at least 150-170 km from the ice front (Fig. 1; Ehlers et al., 2011), thus within the forebulge of the ice sheet.

The stress field evolution within the northern European Alpine foreland, including the study region, has been studied for decades. The compressional stress field has had similar stress parameters since ~2 Ma (Coubal et al., 2015 and references therein) and is known as the Wallachian tectonic phase (Hippolyte and Sandulescu, 1996). The orientation of the maximal principal stress (σ_1) is ~NW-SE and has been probably interrupted by several episodes of stress relaxation. The present-day principal stress in the area is determined from focal mechanisms of micro-earthquakes to be oriented nearly parallel to the SMF (NNW-SSE) (e.g. Špaček et al., 2006). There is also sparse microseismicity and rare light historical earthquakes (with maximum intensity I = 7 MSK in 1895), though there is large uncertainty to ascribe them to a specific fault (see Fig. 1c; Guterch and Lewandowska-Marciniak, 2002). However, it suggests that there is still a potential seismic threat to the region.

3. Methods

3.1. Trenching

We excavated 9 trenches across and 9 trenches parallel to the fault near the village of Bílá Voda in northeastern Czech Republic with a backhoe (Fig. 2). The faces of the one-meter-wide trenches were cleaned, gridded at half-meter intervals, and then photographed for construction of photomosaics of each trench face. The trenches were logged in the field in detail onto millimetric paper. The locations of all trenches were surveyed with a total station tied to geodetic benchmarks.

3.2. Dating

Chronological control for the sediments displaced by the fault, as well as the sediment that caps the fault, was provided by four dating techniques: ^{14}C, Cosmogenic Radionuclide (CRN) dating, Optically Stimulated Luminescence (OSL) and Infra-Red Stimulated Luminescence (IRSL). Results from these techniques provide a framework for development of the site chronology (Table 1). There is broad concordance in age within and between the different techniques, though with some complexity in places (see Supplementary section S2 Chronology).

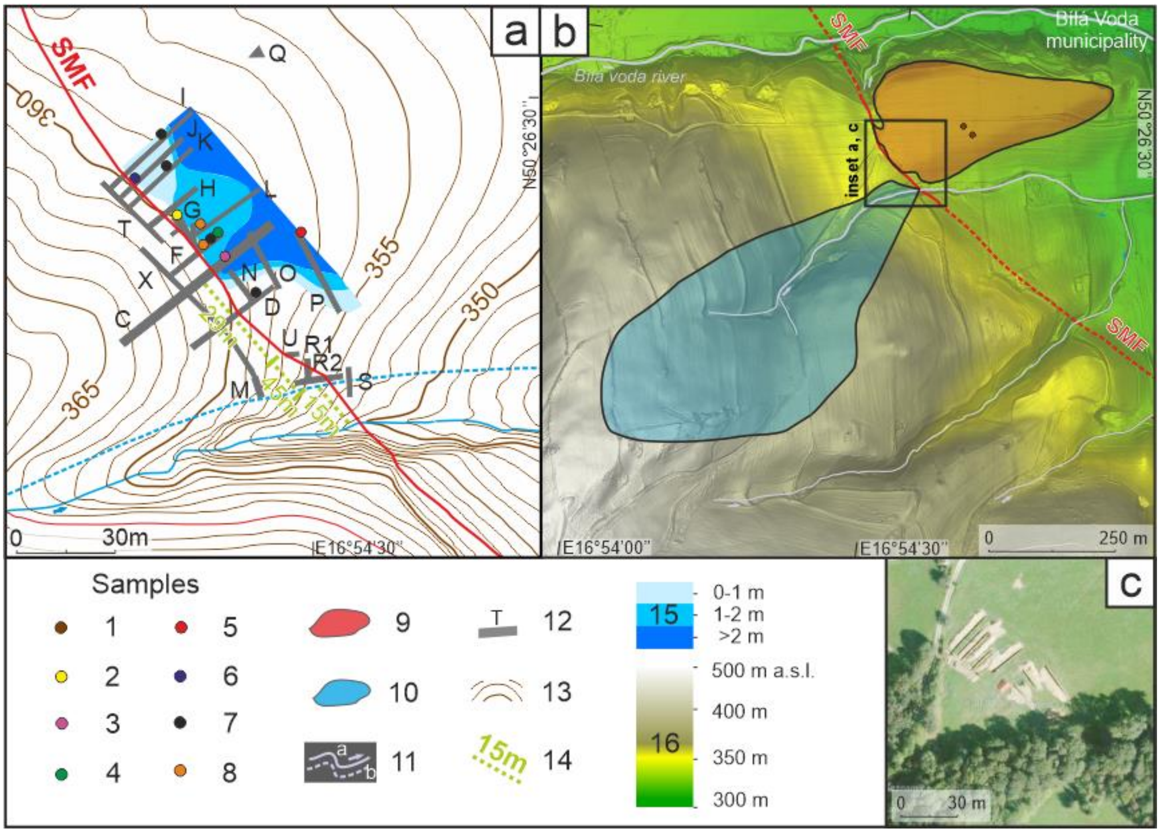

Fig. 2. a) Contour lines map of the trenching site. Sample positions and results of all dating methods on the isopach map of the alluvial fan deposits derived from the trenches, for results see Tab. 1; b) Relief map of the trenching site based on LIDAR data DEM. Note the alluvial fan and its probable source valley; c) Aerial photo of the site from 2012 (source: www.mapy.cz; accessed 03 Jun 2020). 1 – reddish soil, 2 – OSL dated sediments, 3 – $IRSL_{225}$ alluvial fan deposits + geliflucted deposits + Holocene deposits, 4 – ^{10}Be dating in alluvial fan deposits, 5 – ^{14}C dated charcoals/bulk, 6 – alluvial fan deposits derived from geophysical survey, 7 – source area of the alluvial fan deposits, 8a – current channel, 8b – inferred feeder channel, 9 – trench, 10 – contour line interval 1 m, 11 – approximate offset measurements, 12 – isopach map of the alluvial fan deposits based on trenches.

Stratigraphy Unit/Material	Dating method	Sample names	Trench wall facing to	Uncalibrated ^{14}C ages (BP)	Calibrated ^{14}C age (cal. yr. BP) or luminescence age	Comment
50-60 Holocene colluvium/polymict material	^{14}C	**Ti 18**	TI SE	375 ± 20	325-498	
		Ti 16	TI SE	790 ± 15	680-726	
		Bila Voda **F 50**	TC NW	845 ± 30	684-791	
		Bila Voda **F 13**, C 11	TF SE	1180 ± 90	932-1282	
		Bila Voda **DJV 4**	TD SE	1190 ± 20	1061-1178	
		Bila Voda **FJV 16**	TF SE	2130 ± 25	2002-2293	
		Bila Voda **DSZ 7**	TD NW	3200 ± 40	3349-3487	
	IRSL$_{225}$	BV15-**13**	TF NW		0.77 ± 0.12 ka	
	^{14}C	BV **Ti 1**	TI SE	3980 ± 15	4413-4518	
		BV **Ti 5**	TI SE	4070 ± 25	4441-4796	
		Ti 3	TI SE	4535 ± 25	5051-5314	
		BV Tk 1	TK SE	2100 ± 15	2001-2116	
fluvial to colluvial layer in recent valley/silty layers	^{14}C	TR 2 1	TR2 W	8200 ± 20	9026-9275	
		TR 1 V	TR1 SE	9660 ± 25	10812-11190	fault sealing layers
		TR 1 VII	TR1 SE	9595 ± 20	10771-11133	
		TR 1 VIII	TR1 SE	9685 ± 20	10889-11197	
100-140 - geliflucted, soliflucted layers/monomict material	^{14}C	*BV **Ti 20***	*TI SE*	*1935 ± 15*	*1821-1926*	
		Ti 8	*TI SE*	*1865 ± 15*	*1723-1824*	
		*Bila Voda **F 18**, E19*	*TF NW*	*1200 ± 60*	*973-1273*	burnt root
		*Bila Voda **F 19**, E20*	*TF NW*	*1080 ± 170*	*690-1295*	burnt root
		*Bila Voda **D 12**, F25*	*TD NW*	*1120 ± 90*	*801-1272*	bioturbation, charcoal in a fault fissure
		*Bila Voda **D1**/0.75m*	*TD SE*	*2510 ± 30*	*2490-2735*	burnt root
	IRSL$_{225}$	BV15-**12**	TF NW		30.6 ± 4.2 ka	
150 – alluvial fan/gravels, sometimes with silty layers	^{10}Be	SMF-P1	TP SW		~13.1 ka *	best fit, most probably represents age of gelifluction
	IRSL$_{225}$	BV15-**11**	TF NW		24.1 ± 3.7 ka	
		BV15-**10**	TF NW		30.8 ± 4.1 ka	
160 – alluvial fan deposits/silty layer	^{14}C	*BV L-**F6**/RES* ■	*TL NW*	*4725 ± 40*	*5323-5581*	? translocation of Holocene organic acids
		*BV L-**F6**/NaOHsol* ■	*TL NW*	*5660 ± 30*	*6318-6530*	
		*BV F **F31**/1.5m* ■	*TF SE*	*7200 ± 30*	*7938-8159*	
	OSL	*Bila Voda 5 (J63) **BV5***	*TC SE*		*2.6 ± 1.2ka*	
		Bila Voda 4 (J60) **BV4**	TC NW		20.1 ± 5.5ka	
	IRSL$_{225}$	BV15-**09**	TF NW		53.2 ± 3.0 ka	
		BV15-**08**	TF NW		53.2 ± 3.0 ka	combined age 06, 07, 08, 09
		BV15-**07**	TF NW		53.2 ± 3.0 ka	
		BV15-**06**	TF NW		53.2 ± 3.0 ka	
170 – alluvial fan deposits/gravels	IRSL$_{225}$	BV15-**05**	TF NW		37.1 ± 3.1 ka	
175 – alluvial fan deposits/silty-sandy layer	OSL	Bila Voda 3 (K58) **BV3**	TC NW		23.2 ± 1.3ka	
190 – alluvial fan deposits/silty layer	^{14}C	*BV F **H18**/2.5m* ■	*TF NW*	*5650 ± 25*	*6320-6494*	? translocation of Holocene organic acids
	IRSL$_{225}$	BV15-**04**	TF NW		54.6 ± 5.8 ka	combined age 03, 04
		BV15-**03**	TF NW		54.6 ± 5.8 ka	
203 – colluvial wedge/silty-sandy layer	^{14}C	BV **Tj 1**	TJ SE	40900 ± 2500	41772-54395	the larger uncertainties are due to the small sample size
215 – within colluvial wedge/silty-sandy layer	OSL	Bila Voda 2 (L56) **BV2**	TC NW		26.5 ± 1.3 ka	
	IRSL$_{225}$	*BV15-**01***	*TF SE*		*14.1 ± 2.4 ka*	
210 – base of alluvial fan/gravels	IRSL$_{225}$	BV15-**02**	TF NW		62.9 ± 6.1 ka	
vertically dragged layer in fault zone /silty layer		Bila Voda G1 **BVG1**	TG		56.4 ± 2.6ka	trench bottom sampled, position projected to TL
		Bila Voda G2 **BVG2**	TG		76.6 ± 6.6ka	

Table 1. Dating results from Bílá Voda trenching site. Calibrated ages of radiocarbon dating (^{14}C) were obtained using OxCal v4.4.4 programme (after Bronk Ramsey, 2009), 2σ uncertainty and the IntCal20 atmospheric curves (Reimer et al., 2020). Optically Stimulated Luminescence (OSL) on quartz dated by GADAM Centre at Silesian University of Technology using OSL-SAR single aliquot regenerative method; CAM (Central Age Model). Infra-Red Stimulated Luminescence (IRSL) post-IR $IRSL_{225}$ dating on feldspar. For details see Supplementary material S2 – Chronology. Sample names marked in bold match the samples in trench logs in Fig. S1.1.

Italics – samples non-used due to discrepancy

* *probably the age of gelifluction process not the layer accumulation, see S.2 section*

■ *sample of mud, but all the other samples for radiocarbon dating are charcoals*

Note: e.g. trench wall NW = facing to the NW

3.2.1. ^{14}C Dating

We applied ^{14}C dating to samples of detrital charcoal and bulk soil samples collected from the various stratigraphic units. The majority of the charcoal was cleaned in D.I. water at the SDSU (San Diego State University) Quaternary Laboratory, hand-picked with a steel needle under a microscope, and sent to the CAMS facility at UCI (University of California in Irvine) for dating using standard protocol. The other charcoal samples were dated at facilities in GADAM center in Gliwice (Poland), Poznań Radiocarbon Laboratory (Poland), and Kyiv Radiocarbon Laboratory (Ukraine). The samples were processed using the standard published protocols of the individual dating laboratories. Calibrated ages of radiocarbon dates (Table 1), reported at 2σ uncertainty, were calculated using the on-line program OxCal v4.4.4 (Bronk Ramsey, 2009) and applying the IntCal20 atmospheric curves (Reimer et al., 2020).

3.2.2. Luminescence Dating

We applied either quartz OSL or single grain K-feldspar IRSL techniques to date sandy sediments in several trenches. Six quartz OSL samples were dated at GADAM Centre in Gliwice, Poland, using conventional multiple-grain aliquots using a SAR protocol. OSL dose rates were based on sediment from collection tubes, and age estimates were calculated using the Central Age Model (Galbraith et al., 1999).

Twelve IRSL samples were collected in Trench F (BV15 codes), and were processed at the University of Sheffield, UK following methods described in Rhodes (2015). Single grains of potassium feldspar in the size range 180-212 µm separated using a “Super-K” (<2.565 gcm^{-3}) approach were dated applying a post-IR IRSL SAR protocol at 225°C, incorporating a pre-heat at 250°C for 60 s and a hot bleach for 40 s IRSL at 290°C (Rhodes, 2015 and references therein). Fading was assessed directly for each grain and by the measurement of additional bedrock cobble samples, and found to be negligible for the 225°C signal. IRSL age estimation was performed in the manner described in Grützner et al. (2017), developed using samples from active tectonic contexts, and which has been shown to provide ages in good agreement with independent age control (Rhodes, 2015). Gamma dose rates were based on in-situ NaI measurements, beta dose rates were calculated based on ICP-MS determinations of U and Th in the sediment, and ICP-OES for K content, an internal K content of 12.5 ± 2.5% was assumed (Huntley and Baril, 1997), cosmic dose rates were based on overburden thickness, and a water content of 15 ± 5% was used. An overdispersion value of 15% was used, based on experience from single grain measurements of quartz (Rhodes et al., 2010). Further technical details are provided in the Supplementary Material section S4 and Tab. S4.1.

3.2.3. Cosmogenic Radionuclide Dating

A depth profile was collected to 2.5 m for cosmogenic exposure dating from a well-preserved part of the alluvial fan (Trench P, Fig. 2a). Samples were processed in the CRN lab at the Scottish Universities Environmental Research Centre (SUERC) using standard quartz purification (Kohl and Nishiizumi, 1992) and chemistry protocols (Corbett et al., 2016). Beryllium isotope analyses were conducted at the accelerator mass spectrometry (AMS) laboratory at SUERC (Xu et al., 2015) and normalized to the NIST standard with assumed ratio of 2.79 x 10^{-11}, which is consistent with the revised standard value and ^{10}Be half-life (Nishiizumi et al., 2007). Samples were background corrected by propagating the AMS uncertainties for the samples and blanks in quadrature (Table S2.2). All information necessary to calculate the age with version 3 of the CRONUS online calculator (https://hess.ess.washington.edu/; Balco et al., 2008) is provided in the Supplemental Material (Table S2.3). The exposure age calculation used the default production rate calibration dataset and time-dependent scaling model of Lal (1991)/Stone (2000).

3.3. Geophysical survey

Electric resistivity tomography (ERT) survey was conducted to study the subsurface geology surrounding the SMF zone at Bílá Voda. We measured 34 profiles. Several measurements aimed to specify trench position due to favorable lithological contrast allowing to trace the exact fault location. Additional ERT profiles were measured during trenching, either to test a hypothesized lithology or facilitate placement of additional trenches. Finally, a series of long profiles, systematically covering the plateau above Bílá Voda, was measured in order to map the extent of the faulted alluvial fan (Fig. 3).

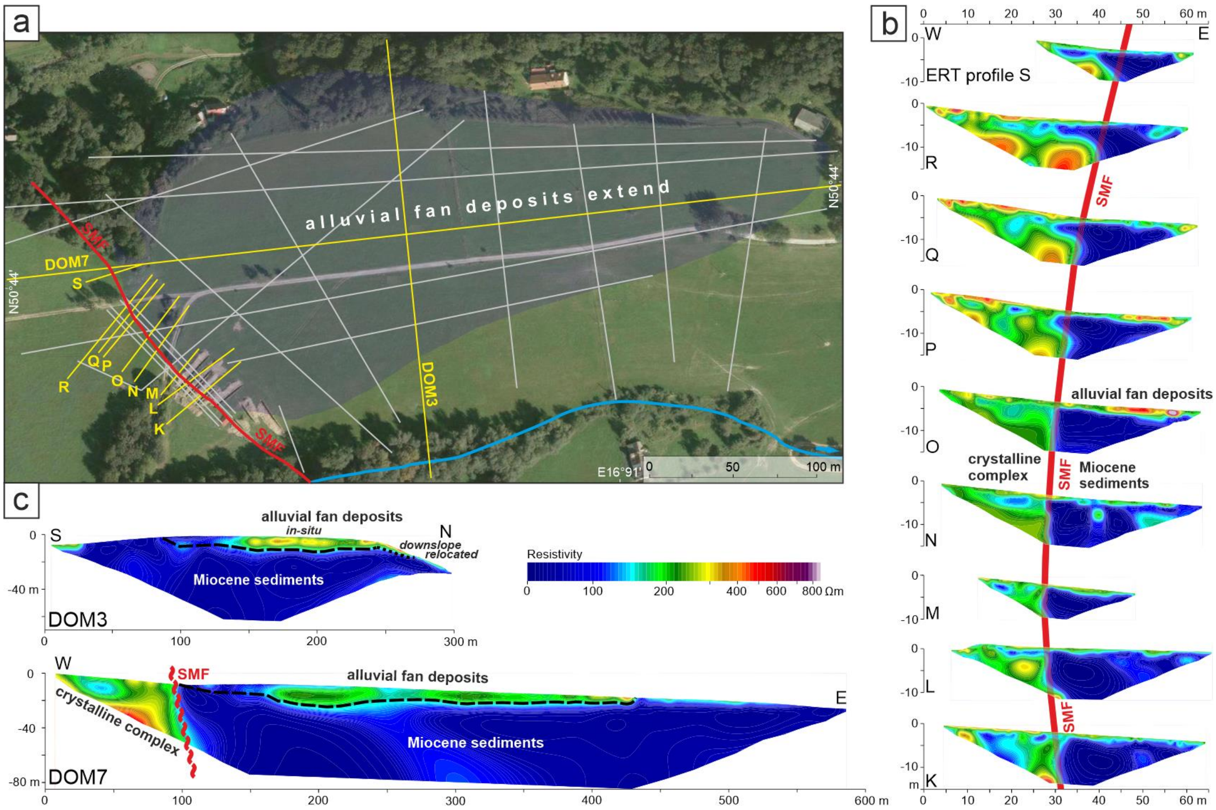

Fig. 3. a) Position of the ERT profiles across the SMF and the alluvial fan on the aerial map; b) ERT profiles K-S crossing the SMF (in yellow on the map). Note the sharp borderline between Miocene clays (NE of the fault) and weathered crystalline rock (SW of the fault), with very significant resistivity difference; c) ERT profiles DOM3 (N-S) and DOM7 (W-E), clearly showing both horizontal and vertical extent of the alluvial fan. Note: All the ERT profiles share the same resistivity scale.

All ERT measurements were performed using ERT device ARES, manufactured by GF Instruments Ltd., with a varying number of multi-electrode cable sections employed. The Wenner – Schlumberger array was used for all profiles as it is considered universal and can detect both vertical and horizontal structures (Loke, 2014).

The measured data were inverted using by Res2DInv64 by Geotomo Software (Loke, 2014). After cleaning the data from the points with excessively high RMS error, the inversion with standard constraints and the 5th iteration were used. Topographic profiles derived from the the LiDAR-based DEM (DMR 5G by Czech Office for Surveying, Mapping and Cadastre) was introduced to the resistivity models during the inversion process. The processed data were visualized in Surfer (Golden software) and adjusted to display unified resistivity scales.

The properties of individual ERT profiles were based on their purpose. The short profiles, in the 1st phase aimed at mapping the subsurface fault trace and lithological units to specify planned trenches position, were more detailed, with electrode spacing as close as 0.8 m and profile length between 39 and 108 m. Final interpretations of these profiles were calibrated according to the geology derived from the trenches (profiles G to S) (Fig. 3b). Secondly, there was a set of long profiles, the purpose of which was to estimate the alluvial fan extent and thickness (Fig. 3a). These profiles were measured using electrode spacing of 5 m, and their length between 165 and 588 m.

4. Results

4.1. Geology exposed by trenches

The trenches exposed a fault zone dividing Paleozoic metamorphic rocks (phyllitic mica schists) in the footwall from Miocene fluvio-lacustrine strata deposits overlain by Quaternary alluvium on the hanging wall (Fig. 4, Fig. S1.1, S2.2., Supplementary Section S1). The fault zone, with the youngest strand exhibiting a strike of 135° and dipping ~75° to the NE, comprises a flower structure (especially pronounced in trenches TC and TD) within the 4-m wide zone of tectonic breccia and fault strands outlined by dark gouge. The fault gouge is composed of at least three generations, as exhibited by various colors and consistencies (massive or schistous clay), which shows repeated faulting (Fig. S1.1, S1.2., S2.2a). Classic features indicative of significant strike-slip motion include rotation of clasts into the fault plane and the complete mismatch of units across the fault.

The Miocene strata on the hanging wall consist of strongly kaolinized clayey silty sand, with the downwarped sediments more strongly folded as they approach the fault zone (see Fig. S1.1). The upper part of the Miocene unit is gelifluted, and very often the gelifluction “lobes” interfinger with the Quaternary alluvial fan deposits, which indicates that the gelifluction acted during and after their deposition. In several trenches (TC, TJ, TK, TL), pieces of tectonic breccia within dark grey fault gouge were also geliflucted and now rest on the geliflucted Miocene surface at a distance of several meters from the fault (Fig. S1.1).

The Quaternary alluvium displays some bedding and channelization with an otherwise relatively massive matrix, indicating an alluvial fan origin, which is consistent with the surface fan morphology. We distinguished several distinct units within the alluvial fan deposits, which could be correlated throughout the trenches (Tab S1.1, Fig. S1.1). Most of them (Units 150, 170, 185, 210, 217) might be best described as matrix-supported intermediate to sandy diamictons with gravel clast content between 5 and 25% and sandy to silty matrix. The average size of the clasts is 5-7 cm and the largest ones are up to 30 cm. The clasts are composed of angular to subangular gneiss, granodiorite and quartz. There are also rare clasts of erratic material that has been brought to the area by an ice-sheet when the last continental glacier reached the study area during the Elsterian 2 glacial epoch, about 400-460 ka BP.

In the upper part of the alluvial fan deposits near the fault, there are finely laminated lenses of beige to grey clayey silt, sand and pebbles (unit 160), and are up to 3 m wide and 35–40 cm thick. The general orientation and dimension of this distinctive sedimentary body was studied in parallel (TG) and perpendicular trenches (TC, TF) trying to resolve the horizontal offset from its source channel. However, no source was found on the footwall. The sedimentary body was exposed in trenches C, F, G, and L, demonstrating that it is >15 m long and 2 m wide oriented parallel to the fault. A plausible interpretation for this unit is a channel that was deflected along the fault due to horizontal displacement, which also implies that lateral displacement was also occurring during fan deposition. After its deposition the lens was tilted and folded and its uphill part was affected by most probably horizontal and reverse faulting as exposed in trench F (Fig. 4, Fig. S1.1, S2.2b).

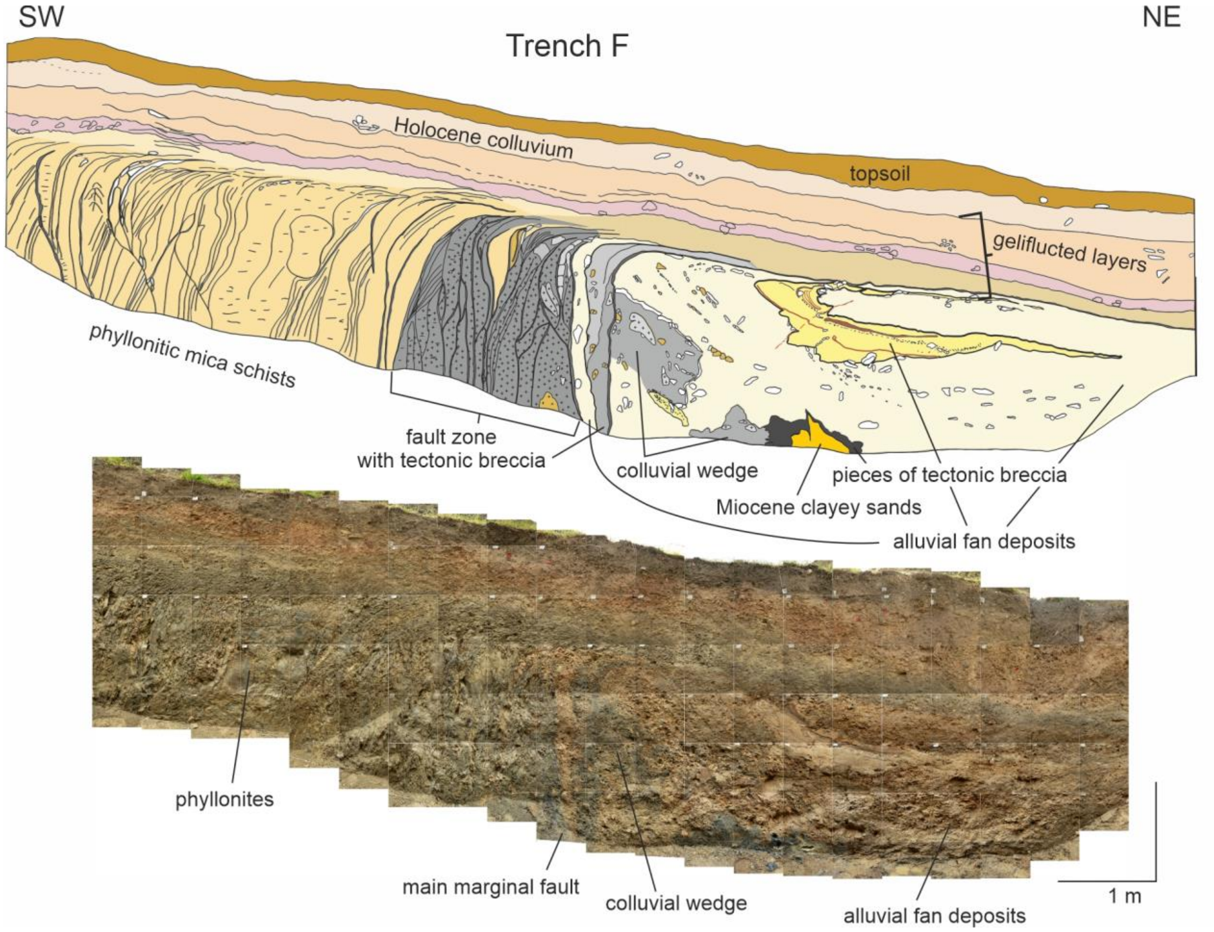

Fig. 4. Log of the SE-facing wall of Trench F and the respective photomosaic. Note the non-mixed gelifluted layers. Colluvial wedges include pieces of tectonic breccia and fault gouge (black clay) from the fault zone, which gives the dark color to the deposit. For sample location from the opposite wall see Fig. S2.2.

Within the alluvial fan deposits adjacent to the fault, there are several wedge-shaped deposits made of matrix-supported, median-grained diamicton with tectonic breccia clasts and fault gouge derived from the fault zone (units 143, 147, 165, 180, 200, and 220). Thus, they are interpreted as colluvial wedges whose material fell from the fault plane being exposed during surface rupturing events. The largest boulder of tectonic breccia that was incorporated into a colluvial wedge measured up to 0.75 m in diameter and was found in the trench D (Fig. S1.1, S1.2), suggesting that this is an indication of the minimum height of the exposed fault plane due to a single earthquake. Gravel clasts are also derived from the hanging wall (upslope) bedrock lithologies (phyllonite, schist, granodiorite).

Several colluvial wedges appear to be superimposed, which we interpret as representing recurring earthquakes. The wedges are deformed themselves as they were successively affected by subsequent earthquake events, as well as by the periglacial surface processes.

On the hanging wall, the bedrock exhibits steeply dipping foliation that is impacted by gelifluction near the ground surface. In the upper 1-1.5 m, there are individual bands of unmixed material 3 to 50 cm thick (typically 10-20 cm) that continue >7 m downslope, and each of the distinct bands could be traced back to the bedrock stratum from which it originated (Fig. 4, Fig. S1.1). These gelifluected layers crossed the fault and flowed over the alluvial deposits. The thickness of bands is similar to what was described in other trenches studied along the SMF at the Vlčice site (Štěpančíková et al., 2010), where layers up to 20 cm thick were interpreted to be deposited by sheet gelifluction and dated to the Late Glacial period based on radiocarbon dating. Thus, gelifluction in this part of Bohemian was limited to the periglacial climate of the late Pleistocene (c.f. Sauer and Felix-Henningsen, 2006), indicating that the alluvial fan, which is overlain by gelifluected material, predates the full glacial conditions of the Last Glacial Maximum (LGM - Marine Isotope Stage (MIS) 2) (Supplementary material S2 Chronology). All the banded solifluected/gelifluected layers are overlain by late Holocene polymict colluvial deposits into which the modern topsoil has developed.

4.2. Age determination of the sediments

Direct dating of the alluvial fan deposits near to the eastern limit of the fan using OSL techniques yielded an age of 25.8±1.6 ka for the alluvial fan deposits in trench C (Fig. S1.1, S2.2, Table 1). A sample of detrital charcoal from a fault-related colluvial wedge overlying the base of the alluvial fan deposits in trench J yielded a calibrated ^{14}C age of $44.2^{+5.5}/_{-2.1}$ ka (Fig. S1.1, S2.1, Table 1). IRSL dating of feldspars from the same deposits indicates that the basal alluvium overlying the Miocene strata date to 63±6 ka, grading up to between 24±3 and 31±4 ka for the top of the fan deposits, all of which show that deposition occurred during MIS 3 and early MIS 2 time (Fig. 4, S1.1; see the discussion of dating results in the Supplementary Section S2).

Strata of silt-rich deposits that locally overlie the geliflucted layers in Trench R, which is located within the valley of the modern channel outside of the alluvial fan deposits, yielded radiocarbon ages as old as cal. yrs 11.15±0.05 ka and confirm the inference for the late Pleistocene age of the gelifluction process. This is consistent with cosmogenic ^{10}Be surface exposure dating that supports an end of gelifluction and surface stability since about ~13 ka (see Supplementary section S2, Tab. S2.3). Applying a simple model to the observed ^{10}Be results, i.e., best fit to data of an exponential profile with density = 2.13 g/cm^3 and attenuation length = 160 g/cm^2, that accounts for pre-depositional exposure (best fit inheritance = 46,211 atoms/g) and assuming no surface erosion, ^{10}Be concentrations are well-fit with an apparent exposure age, corrected for topographic shielding, of ~13 ka (Fig. 5, Tab. S2.2., S2.3). However, this is a minimum limiting age if the surface was eroded by gelifluction in the late Pleistocene. Notably, the ~11 ka strata (dated by ^{14}C) cap the fault, demonstrating the lack of Holocene motion on the SMF at this location. Younger Holocene colluvium in other trenches, which was dated by radiocarbon and yielded ages of 0.3 to 5.3 ka, was also unfaulted.

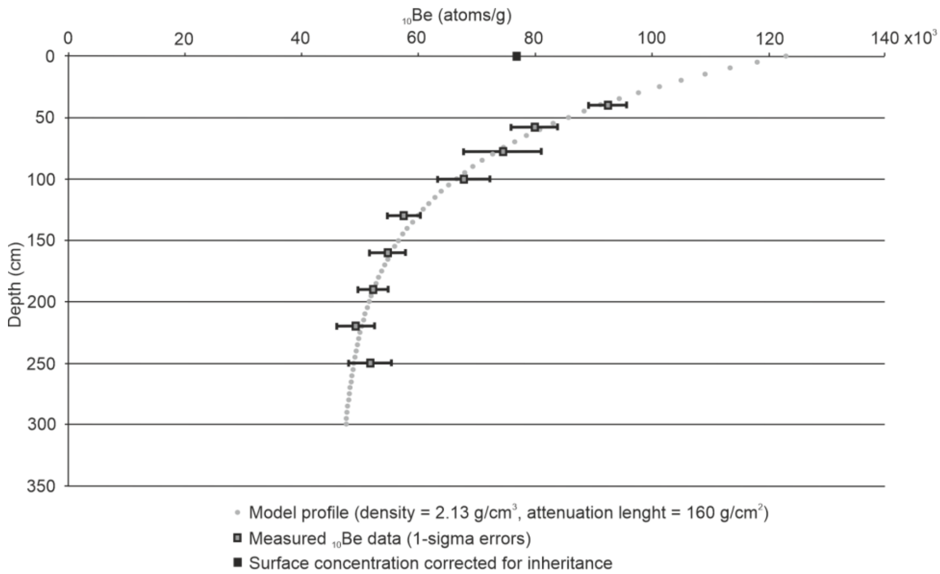

Fig. 5. Depth profile showing results of CRN dating of fan surface.

4.3. Alluvial fan offset

The 3-dimensional distribution of the alluvial fan deposits was explored through a network of trenches (Fig. 2). The thickness of the fan deposits varies systematically throughout the site, with the greatest thickness at the inferred apex of the paleo-fan and thinning with distance from the apex. The apex thickness of the youngest part of the fan as exposed in the trenches ranges between 2 and 3 m, with the majority of the fan deposit less than 1.5 m near the fault (Fig. S1.1).

Altogether, the well-defined apex, along with the distribution of fan deposits defined by trenches and geophysical survey showed that alluvial fan is completely beheaded (Fig. 2 and Fig. 3). When searching for a possible "feeder channel" as the source of the alluvial fan deposits to obtain the sense and rate of slip of this fault by fault-parallel trenches and ERT survey, no such channel appeared on the southwest side of the fault northwest of the fan apex for at least 100 m. As well, fault-parallel trenches excavated southwest of the fault (Trench T and Trench X; Fig. 2) exposed only Paleozoic schist across the entire site. The top of the schist is remarkably smooth and is capped by the gelifluction layers that originated a few meters upslope (Fig. 4, Fig. S1.1), so any paleo-channel cut into the schist would be readily apparent unless the footwall was considerably eroded by at least 2 m more than the hanging wall, which we consider unlikely. In contrast, a small drainage of the appropriate size for the fan deposit is present about 45-60 m to the southeast of the fan. Based on these observations, the most plausible interpretation is that the alluvial fan is left-laterally displaced by a few tens of meters (Fig. 2), which is consistent with geomorphic observations of left-laterally offset valley walls on the SMF (Štěpančíková and Stemberk, 2016).

To estimate the amount of late Quaternary left-lateral motion, we reconstructed the apex to the small channel to the southeast (Fig. 2). Using a straight-line projection of the average channel trend results in about 45 m of reconstructed slip. Taking the apex to the center of the currently incised drainage adds another 10-15 m, although it is likely that this is an overestimate because the drainage curves to the southeast, whereas the alluvial fan appears to have spilled along the same trend as the upslope portion of the channel. For an estimate of the minimum displacement, we take the elevation of the base of the alluvium at the apex and reconstruct it horizontally to the same elevation contour in the modern topography at the source drainage, and allowing for as much as a half-meter of vertical slip, results in 29 m of estimated slip (Fig. 2).

Based on these reconstructions, we estimate that the fan apex is left-laterally offset by 29 to 45 m, with a maximum possible displacement of about 60 m if the apex is reconstructed to the center of the modern drainage. As the actual value could fall anywhere in between these values, and because we consider the maximum value to be an overestimate, we use a best estimate of 37±8 m of left-lateral slip for the ~24-63 ka alluvial fan. Thus, we calculate the best estimate of the average long-term strike-slip rate is about $0.85^{+1.0}/_{-0.4}$ mm/yr.

Several trenches were also excavated close to the modern valley (Trench M, U, R1, R2, and Trench S) in order to both search for remnants of the alluvial fan and also to search for younger faulted deposits. Trench R1 (Fig. 2, Fig. S2.1) exposed faulted alluvium sealed by unfaulted fine-grained silt-rich strata that yielded calibrated radiocarbon ages on charcoal of about 11 ka, indicating that the last period of motion was greater than 11,000 years ago. This is consistent with observations in all trench exposures, which showed a pattern of gelifluted layers capping the fault (Fig. S1.1): this consistent pattern is surprising when the amount of late Pleistocene displacement is considered. In fact, this implies that the 37±8 m of left lateral displacement occurred in the period between about 11 ka BP and 24-63 ka.

5. Discussion

5.1. Activity and Earthquake Potential of the Sudetic Marginal fault

The Sudetic Margin fault zone exhibits geomorphic expression for about 140 km, which we take as the expected fault length as well as the maximum rupture length that the fault could sustain in a single earthquake. However, there are two 3.5-4 km restraining steps or double bends that may segment the fault into 35-65 km segments, and if some or all earthquakes rupture only a single segment, then the associated earthquakes would be smaller. Considering a seismogenic depth of ~15 km, and applying the relationship between fault area and earthquake magnitude (Wells and Coppersmith, 1994; Leonard, 2010), we estimate that the fault could have generated earthquakes as large as Mw7.3 when active in the late Pleistocene if the entire fault ruptured in a single event. Alternatively, earthquakes in the magnitude range of Mw6.7 (35 km) to Mw7 (65km) may have occurred if individual segments failed independently. Mw7.3 earthquakes typically host average and maximum displacements of ~1.8 m and 3.1 m, respectively, which implies that the 37±8 m of the observed displacement could have been accommodated in as few as 10 to 15 such earthquakes assuming maximum displacement, or as many as 16-25 earthquakes if only average displacement. In contrast, assuming that the Bílá Voda segment ruptured independently in Mw6.7 earthquakes that are expected to have average displacements of just under a meter, it is possible that close to 50 moderate events were required to produce the observed displacement. In any case, such an earthquake today would likely be quite destructive as most buildings are not designed for large earthquakes in this region of Central Europe.

A slip rate in the 1 mm/yr range is anomalous for Central Europe where geodetic strain rates are low and close to zero. Whether another large earthquake is possible on this fault in the near future is unknown, but the pattern of a relatively high displacement rate at the end of Pleistocene followed by an essentially zero Holocene rate demands an explanation. As the period of fault activity is also the same general time-frame during which glaciers covered parts of Europe, and the period of inactivity coincides with the absence of continental-scale glaciation, in the next section we explore the effects of ice-loading on local and regional stress to test whether this may have played a role in the faults' activity.

5.2 Modeling of ice-loading as a possible cause of fault acceleration

Most of the documented Late Pleistocene activity on the SMF coincides with time when ice covered the European continent or was receding, and the SMF was in the area of Fennoscandian ice sheet forebulge. Based on our geological data, after the end of Pleistocene time, surface movement on the fault ceased and no observable displacement has occurred since 11 ka. Holocene inactivity is also in agreement with our previous paleoseismic survey 20 km south of the Bílá Voda study site (Štěpančíková et al., 2010). Also, it agrees with the modern maximum principal stress (σ_1), which is oriented nearly parallel to the SMF (NNW-SSE) (e.g. Špaček et al., 2006), thus being unfavorable for significant fault motion. The recorded historical seismicity is represented only by light earthquakes with maximum intensity I = 7 MSK (Guterch and Lewandowska-Marciniak, 2002; Fig. 1). These observations suggest a possible causal relationship between ice loading and the observed late Pleistocene fault motion.

We hypothesize that the glacially induced stresses in the forebulge of the Weichselian ice sheet may have caused a change in the local stress field, which would have rotated σ_1 and induced the observed left-lateral motion of the SMF, or at least caused an acceleration in the rate of fault motion. If that was the case, then removal of the ice would have caused relaxation of the stress field and locking of the fault in the Holocene, which would explain the lack of Holocene motion.

To test this hypothesis, we modeled local changes in stress along the SMF due to nearby glacial loading and unloading. In the absence of reliable estimates of paleo (or modern) absolute stress magnitudes, we cannot determine whether induced stress changes were sufficient to rotate σ_1 into favorable orientation. We can, however, estimate the magnitude, orientation, and timing of stress perturbations resolved on the SMF to determine whether glacial loading and unloading is a plausible mechanism for explaining the observations from the Bílá Voda trench site.

To this end, we calculate stress using a two-layer model of a flexing elastic plate, representing the lithosphere, overlying a viscoelastic halfspace, representing the asthenosphere, in response to a changing surface load (Luttrell et al., 2007; Luttrell and Sandwell, 2010; see Supplementary Section S3). The load shape over time is derived from models of northern hemisphere ice sheet geometry since 50 ka, interpolated to 1000-yr time intervals to represent the history of glaciation (Zweck and

Huybrechts, 2005; Ehlers et al., 2011). The model convolves the analytically derived 3-D deformation due to a surface point load (Green's function) with the actual load shape as it varies over time (Luttrell and Sandwell, 2010). The resulting 4-D stress tensor represents the stress changes induced by ice sheet loading, relative to present day ice-free conditions. This stress field is then resolved into the changes in normal ($\Delta\tau_n$) and shear ($\Delta\tau_s$) stress components acting on a hypothetical fault plane within the lithosphere with a specified strike, dip, and sense of slip (rake). The change in Coulomb failure stress on the fault plane ($\Delta\tau_c$) is calculated as

$$\Delta\tau_c = \Delta\tau_s + \mu_f \Delta\tau_n, \qquad (1)$$

where μ_f represents the coefficient of friction and a positive change in Coulomb stress promotes failure on the specified fault plane in the specified sense of slip (e.g., King et al., 1994).

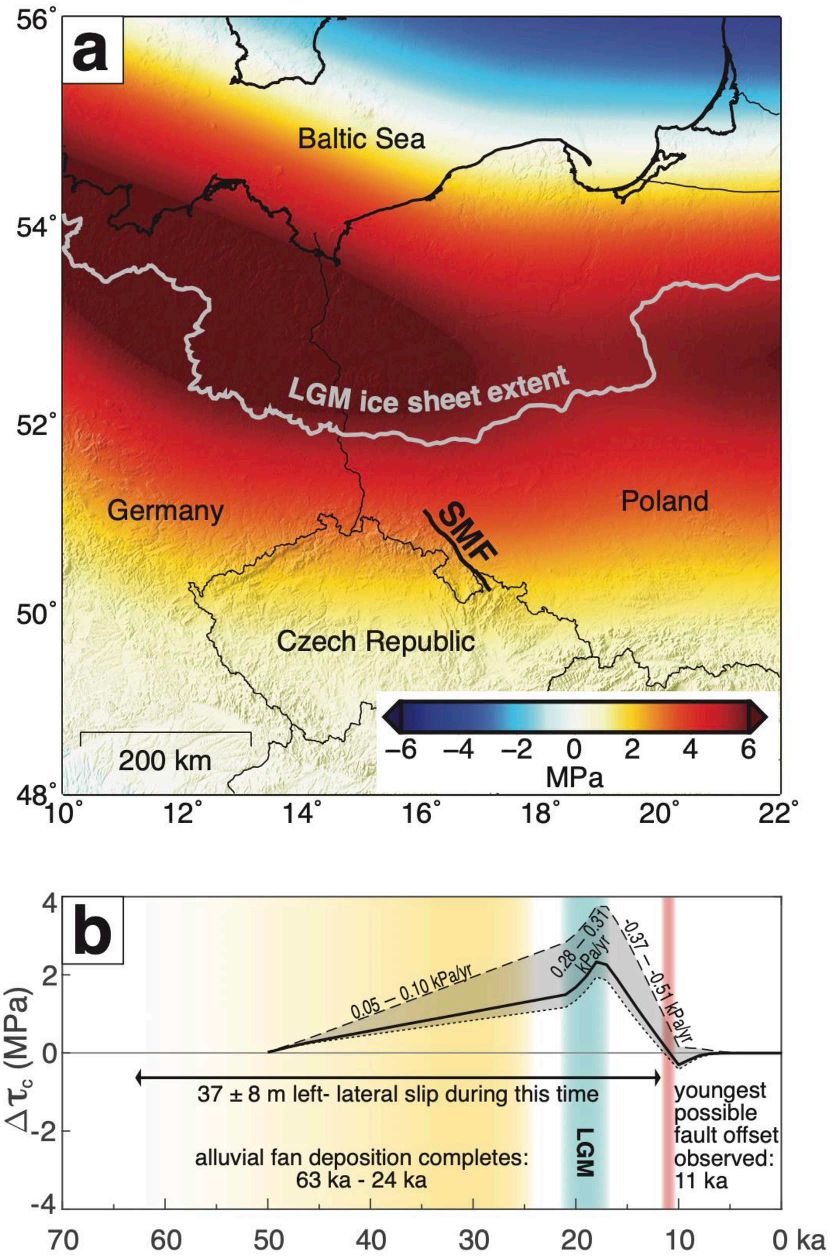

Fig. 6. A) Predicted change in Coulomb failure stress at LGM (18 ka), relative to ice-free conditions, on a left-lateral fault plane with same orientation as SMF. Positive (negative) change in Coulomb failure stress promotes (inhibits) failure. B) Range of Coulomb failure stress change over time along the SMF (gray shading), with northern end (dashed), southern end (dotted), and Bílá Voda location (solid black line) shown. Range of stress accumulation rates during ice sheet buildup, LGM, and ice sheet retreat are indicated. Note both the highest Coulomb failure stress and the highest rate of Coulomb failure stress accumulation occur during LGM (blue shading). Ice sheet extent is adopted from Ehlers et al. (2011). Timing of latest alluvial fan deposition (tan shading) and its latest fault offset (red shading) is from this study.

The modeling results demonstrate that for most of the episode of last glaciation, the SMF lies along the edge of the flexural bulge associated with the continental ice sheet, which tends to promote slip on the SMF (Figure 6). As the ice sheet advances, the flexural bulge shifts southward and Coulomb stress increases along the SMF. As the ice sheet retreats, the flexural bulge shifts northward, which reduces the Coulomb stress (Supplemental movie S3.M1).

We find that Coulomb stress along the SMF gradually increased by ~1 – 2 MPa from 50 – 25 ka at a rate of 0.05 – 0.1 kPa/yr. It then rapidly increased by an additional ~1 MPa during the time leading up to the LGM at a rate of 0.28 – 0.31 kPa/yr. As the ice sheet retreated, the Coulomb stress rapidly decreased at a rate of -0.37 – -0.51 kPa/yr from 17 – 11 ka (Figure 6b). Our modeling suggests that the most likely time for rapid left-lateral SMF reactivation over the last 50 ka is between ~21 ka – 17 ka. This is consistent with our observations of substantial left lateral offset between the end of alluvial fan deposition ~24 ka and 11 ka (fault sealing layers), and demonstrates that glacial loading is likely to have contributed substantially to the fault activity observed at the Bílá Voda trench site. We tested the robustness of these interpretations by calculating the results for a wide range of model parameters (see Supplementary Section S3). The results described here conservatively represent the lowest reasonable stress changes, though we note that the absolute stress changes could reasonably be higher by up to a factor of 2. We also note these results are consistent with other studies of glacially induced stress changes in originally unfavorably oriented stress fields (e.g., Steffen & Steffen, 2021).

While the local two-layer model presented here is certainly a simplification of the actual rheological structure of the earth, it is reasonable for testing the plausibility of the glacial reactivation hypothesis presented here. A full dedicated global glacial isostatic adjustment model (e.g., Wu et al. 2021 and references therein) is valuable when conducting large-scale simulations of ice sheet growth and may in the future provide context for the relationship between fault reactivation in this part of central Europe and other sections of the ice sheet, or provide more refined predictions of the expected timing of fault activity in this area. However, as we are focused on the paleostress perturbations to a single 140 km long fault off the ice sheet margin and conditions appropriate to that location, the errors introduced by neglecting more intricate 3-D rheology variations or spherical geometry are second order relative to both the uncertainties in our observations and the range of predicted stress values presented here. We are confident that the model non-uniqueness described by our conservative range of considered parameters adequately captures the full range of glacial stress perturbations likely to have been experienced by this fault, and that our interpretations are therefore robust.

5.3. An interval slip rate

As discussed above, the 37±8 m of left lateral displacement occurred in the period between about 24-63 ka and 11 ka BP. If correct, this indicates that the slip rate was $1.1^{+2.3}/_{-0.6}$ mm/yr during the latest Pleistocene, and has been essentially zero during the Holocene, although that does not mean that the fault could not move again in the future. However, the $1.1^{+2.3}/_{-0.6}$ mm/yr late Pleistocene slip rate assumes constant loading over the period when ice was present, but from the modeling, it is clear that the effect of ice load was not constant over the entire timeframe between the end of alluvial fan deposition at about 24 ka, and the end of the Pleistocene at about 11 ka, after which there has not been any displacement. For the purposes of estimating a plausible slip rate for this period, we use the timing of the beginning of rapid ice growth at about 28 ka for the initiation of fault motion during and after fan growth. Similarly, we use the end of the Younger Dryas at about 12 ka as the likely end of the period of ice-driven fault slip because the ice-shield retreated rapidly after this time. This calculates to an average rate in this period of 1-2.8 mm/yr, but if most of the displacement occurred when the ice load was at a maximum between about 21 and 18 ka, the interval rate during this period could have been higher. Notably, the 10-15 earthquakes required to have produced the observed displacement may not have been periodic in their temporal distribution, as the applied stress first increased and then decreased over this period, so the recurrence interval may have also been shortest during the period of maximum ice load.

6. Conclusion

We studied late Quaternary activity of the Sudetic Marginal fault (SMF) by extensive paleoseismic trenching (9 fault-crossing and 9 fault-parallel trenches), geophysical survey (34 ERT profiles), and radiometric dating in the study site near the town of Bílá Voda in northeastern Bohemian Massif (Czech Republic). The SMF has experienced alternating kinematics since the Paleozoic, but in this study, we exposed the SMF as a subvertical fault zone striking 135° – 150°/75° NE with a left-lateral sense of slip. The strike-slip kinematics is suggested by a flower structure within the 4-m wide zone of tectonic breccia and fault gouge, and by the juxtaposition of Paleozoic crystalline rocks (phyllites, schists, granitic aplite) against Miocene strata and late Pleistocene alluvial fan deposits offset by the fault. We dated the alluvial fan by ^{14}C, OSL, IRSL, and ^{10}Be methods, which indicate that the alluvium accumulated between 63 and 24 ka. We estimate displacement by reconstructing the fan apex to its probable (and only plausible) source drainage, resulting in 37±8 m of left lateral offset. As there has been no Holocene motion observed, we assume that all of this displacement occurred during and after deposition of the alluvial fan deposits, resulting in a late Pleistocene slip rate of $1.1^{+2.3}/_{-0.6}$ mm/yr, dropping to zero in the Holocene.

As the site lies ~150 km south from the Late Pleistocene Weichselian maximum (~20 ka) ice sheet front, we tested a hypothesis of causal relationship between the slip rate acceleration and ice loading by modeling. The models of related lithosphere flexure suggest failure on the SMF was promoted by the presence of the ice sheet, relative to an ice-free state, while Coulomb stress on the SMF increased by ~1 MPa during the time leading up to the LGM, and then rapidly decreased as the ice sheet retreated. Thus, the most favorable time for a glacially-loaded lithosphere to induce rapid left-lateral reactivation on the SMF over the last 50 ka would be during the glacial maximum ~21-17 ka, with most or all displacement likely occurring between about 28 and 12 ka; the resulting slip rate in that period may have been much higher than the average $1.1^{+2.3}/_{-0.6}$ mm/yr rate. Thus, it implies that although the tectonics and seismicity in northern Czech Republic/southern Poland is influenced by the Alpine collision, glacial isostatic adjustment was an extra trigger which altered the local stress field, promoted the reactivation of the SMF and led to its accelerated motion. Our work based on field evidence support the results of an increasing number of studies (Houtgast et al., 2005; Brandes et al., 2015) on late Quaternary faults in the former Fennoscandian ice sheet forebulge that were affected by the phenomenon of near-field ice loading and its attendant changes in stress, which resulted in a pronounced seismicity increase and higher slip rates in late Pleistocene than in Holocene. We note that this is a different effect from the direct removal of ice load, which occurs north of the ice front during glacial retreat which causes postglacial slip and suggests even historical deglaciation seismicity (Steffen et al., 2021).

The SMF is the southernmost and first glacially triggered fault described in the Czech Republic and Poland. Our findings motivate further geoscientific investigations at other parts of the SMF (especially in the north) to test the hypothesis that the whole SMF was glacially triggered during the last glaciation and ruptured as the whole or in parts. Our findings of the fault acceleration during the end of Pleistocene in contrast to no Holocene displacements have also major implications for seismic hazard assessment, which will have to consider that the substantial motion on such faults might be a consequence of stress conditions that no longer exist.

Acknowledgements: The research was supported by the Czech Science Foundation projects No. 205/08/P521, No. P210/12/0573, and by the Czech Ministry of Education, Youth and Sports project No. LH12078. We thank the staff of the AMS Laboratory at the Scottish Universities Environmental Research Centre (SUERC) for support during beryllium isotope analyses. Lucie Nováková, Miloš Briestenský, Věra Primasová, Monika Hladká, Petra Bestajovská, and Jana Šreinová are acknowledged for help in the field, and for technical and graphical support. We thank Miroslav

Kocián, the mayor of Bílá Voda municipality in the study site, for all-embracing support during several field campaigns. We are also thankful to the Holger Steffen and an anonymous reviewer for their suggestions which helped to improve the manuscript.

References

Arvidsson, R., 1996. Fennoscandian earthquakes: Whole crustal rupturing related to postglacial rebound. Science, 274, 1, 744-746. https://doi.org/10.1126/science.274.5288.744.

Badura, J., Przybylski, B., Zuchiewicz, W., 2004. Cainozoic evolution of Lower Silesia, SW Poland: a new interpretation in the light of sub-Cainozoic and sub-Quaternary topography. Acta Geodyn. Geomater., 1(3), 7-29.

Badura, J., Zuchiewicz, W., Štěpančíková, P., Przybylski, B. Kontny, B., Cacoń, S., 2007. The Sudetic Marginal Fault: A young morphotectonic feature at the NE margin of the Bohemian Massif, central Europe. Acta Geodyn. Geomater., 4(4), 7-29.

Balco, G., Stone, J., Lifton, N., Dunai, T., 2008. A complete and easily accessible means of calculating surface exposure ages or erosion rates from ^{10}Be and ^{26}Al measurements. Quaternary Geochronology, 3, 174-195. https://doi.org/10.1016/j.quageo.2007.12.001.

Birkenmajer, K., Jeleńska, M., Kądziałko-Hofmokl, M., Kruczyk, J., 1977. Age of deep-seated fractures zones in Lower Silesia (Poland), based on K-Ar and paleomagnetic dating of Tertiary basalts. Rocznik Polskiego Towarzystwa Geologicznego – Annales de la Société Géologique de Pologne, Kraków, XLVII, 4, 545-552.

Brandes, C., Steffen, H., Steffen, R., Wu, P., 2015. Intraplate seismicity in northern Central Europe is induced by the last glaciation. Geology, 43(7), 611-614. https://doi.org/10.1130/G36710.1.

Bronk Ramsey, C.B., 2009. Bayesian analysis of radiocarbon dates. *Radiocarbon, 51*(1), 337-360. https://doi.org/10.1017/S0033822200033865.

Byerlee, J.D., 1993. Model for episodic flow of high-pressure water in fault zones before earthquakes. Geology 21, 303-306. https://doi.org/10.1130/0091-7613(1993)021<0303:MFEFOH>2.3.CO;2

Corbett, L.B., Bierman, P.R., Rood, D.H., 2016. An approach for optimizing in situ cosmogenic ^{10}Be sample preparation. Quaternary Geochronology, 33, 24-34. https://doi.org/10.1016/j.quageo.2016.02.001.

Coubal, M., Málek, J., Adamovič, J., & Štěpančíková, P. (2015). Late Cretaceous and Cenozoic dynamics of the Bohemian Massif inferred from the paleostress history of the Lusatian Fault Belt. Journal of Geodynamics, 87, 26-49. http://doi.org/10.1016/j.jog.2015.02.006

Danišík, M., Štěpančíková, P., Evans, N., 2012. Constraining long-term denudation and faulting history in intraplate regions by multi-system thermochronology – an example of the Sudetic Marginal Fault (Bohemian Massif, Central Europe). Tectonics, 31, Tc2003, 19pp. https://doi.org/10.1029/2011TC003012.

Ehlers, J., Gibbard, P. L., Hughes, P. D., eds., 2011. Quaternary Glaciations – Extent and Chronology, A closer look. Developments in Quaternary Science, Elsevier, 15, 37-46.

Farr, T. G., eds., 2007. The Shuttle Radar Topography Mission. Rev. Geophys., 45, RG2004. https://www2.jpl.nasa.gov/srtm, Accessed date: 12 Nov 2018. https://doi.org/10.1029/2005RG000183.

Galbraith, R.F., Roberts, R.G., Laslett, G.M., Yoshida, H., Olley, J.M., 1999. Optical dating of single and multiple grains of quartz from Jinmium rock shelter, northern Australia: Part I, experimental design and statistical models. Archaeometry, 41(2), 339-364. https://doi.org/10.1111/j.1475-4754.1999.tb00987.x.

Grützner, C., Carson, E., Walker, R.T., Rhodes, E.J., Mukambayev, A., Mackenzie, D., Elliott, J.R., Campbell, G., Abdrakhmatov, K., 2017. Assessing the activity of faults in continental interiors: palaeoseismic insights from SE Kazakhstan. Earth Planet. Sci. Lett., 459, 93-104. https://doi.org/10.1016/j.epsl.2016.11.025.

Guterch, B., Lewandowska-Marciniak, H., 2002. Seismicity and seismic hazard in Poland. Folia Quaternaria 73, 85-99.

Hampel, A., Hetzel, R., Maniatis, G., 2010. Response of faults to climate-driven changes in ice and water volumes on Earth's surface. Philosophical Transactions of the Royal Society A: Mathematical, Physical and Engineering Sciences, 368(1919), 2501-2517. https://doi.org/10.1098/rsta.2010.0031.

Hippolyte, J. C., & Sandulescu, M. (1996). Paleostress characterization of the ''Wallachian phase'' in its type area (southeastern Carpathians, Romania). *Tectonophysics, 263*(1-4), 235-248. http://doi.org/10.1016/S0040-1951(96)00041-8

Houtgast, R.F., Van Balen, R.T., Kasse, C., 2005. Late Quaternary evolution of the Feldbiss Fault (Roer Valley Rift System, the Netherlands) based on trenching, and its potential relation to glacial unloading. Quaternary Science Reviews 24, 489-508. https://doi.org/10.1016/j.quascirev.2004.01.012.

Huntley, D. J., Baril, M., 1997. The K content of the K-feldspar being measured in optical dating or in thermoluminescence dating. Ancient TL, 15, 11-13.

Hürtgen, J., Reicherter, K., Spies, T., Geisler, C., Schlittenhardt, J. (2021): The Paleoseismic Database of Germany and Adjacent Regions PalSeisDB. V. 1.0. GFZ Data Services. https://doi.org/10.5880/fidgeo.2020.040

James, T. S., Bent, A. L., 1994. A comparison of eastern North American seismic strain-rates to glacial rebound strain-rates. Geophysical Research Letters, 21(19), 2127-2130. https://doi.org/10.1029/94GL01854.

King, G. C. P., Stein, R. S., Lin, J., 1994. Static stress changes and the triggering of earthquakes, Bull. Seismol. Soc Am., 84(3), 935-953.

Kley, J., Voigt, T., 2008. Late Cretaceous intraplate thrusting in central Europe: Effect of Africa-Iberia-Europe convergence, not Alpine collision. Geology, 36(11), 839-842. https://doi.org/10.1130/G24930A.1.

Kohl, C., Nishiizumi, K., 1992. Chemical isolation of quartz for measurement of in-situ-produced cosmogenic nuclides. Geochim. Cosmochim. Acta, 56, 3583-3587. https://doi.org/10.1016/0016-7037(92)90401-4.

Krzyszkowski, D., Pijet, E., 1993. Morphological effects of Pleistocene fault activity in the Sowie Mts., southwestern Poland, Zeitschr. Geomorph., 4, 243-259.

Krzyszkowski, D., Przybylski, B., Badura, J., 2000. The role of neotectonics and glaciation on terrace formation along the Nysa Kłodzka River in the Sudeten Mountains (southwestern Poland), Geomorphology, 33, 149-166. https://doi.org/10.1016/S0169-555X(99)00123-3.

Lal, D., 1991. Cosmic ray labeling of erosion surfaces: in situ nuclide production rates and erosion models. Earth Planet. Sci. Lett., 104, 424-439. https://doi.org/10.1016/0012-821X(91)90220-C.

Leonard, M., 2010. Earthquake Fault Scaling: Self-Consistent Relating of Rupture Length, Width, Average Displacement, and Moment Release. Bull. Seismol. Soc Am., 100(5A), 1971-1988. https://doi.org/ 10.1785/0120090189

Loke, M.H., 2014. Tutorial: 2-D and 3-D electrical imaging surveys. Geotomo Software, Malaysia.

www.geotomosoft.com.

Luttrell, K., Sandwell, D., 2010. Ocean loading effects on stress at near shore plate boundary fault systems. J. Geophys. Res., 115, B08411. https://doi.org/10.1029/2009JB006541.

Luttrell, K., Sandwell, D., Smith-Konter, B., Bills, B., Bock, Y., 2007. Modulation of the earthquake cycle at the southern San Andreas fault by lake loading. J. Geophys. Res., 112, B08411. https://doi.rog/10.1029/2006JB004752.

Nishiizumi, K., Imamura, M., Caffee, M., Southon, J., Finkel, R., McAninch, J., 2007. Absolute calibration of ^{10}Be AMS standards. Nucl. Instrum. Methods Phys. Res. B Beam Interact. Mater. At., 258, 403-413. https://doi.org/10.1016/j.nimb.2007.01.297.

Oberc, J., 1991. Systems of main longitudinal strike-slip faults in the vicinity of the Gory Sowie Block (Sudetes), Kwart. Geol., 35, 403-420.

Reimer, P., Austin, W., Bard, E., Bayliss, A., Blackwell, P., Bronk Ramsey, C., . . . Talamo, S. (2020). The IntCal20 Northern Hemisphere Radiocarbon Age Calibration Curve (0–55 cal kBP). Radiocarbon, 62(4), 725-757. https://doi.org/10.1017/RDC.2020.41.

Rhodes, E.J., 2015. Dating sediments using potassium feldspar single-grain IRSL: initial methodological considerations. Quaternary International, 362, 14-22. https://doi.org/10.1016/j.quaint.2014. 12.012.

Rhodes, E.J., Fanning, P.C., Holdaway, S.J., 2010. Developments in optically stimulated luminescence age control for geoarchaeological sediments and hearths in western New South Wales, Australia. Quaternary Geochronology, 5, 348-352. https://doi.org/10.1016/j.quageo.2009.04.001.

Sauer D., Felix-Henningsen P., 2006. Saprolite, soils, and sediments in the Rhenish Massif as records of climate and landscape history. Quaternary International, 156-157, 4-12. https://doi.org/10.1016/j.quaint.2006.05.001.

Scheck, M., Ulf, B., Otto, V., Lamarche, J., Banka, D., Pharaoh, T., 2002. The Elbe Fault System in North Central Europe – a basement controlled zone of crustal weakness. Tectonophysics, 360, 281-299. https://doi.org/10.1016/S0040-1951(02)00357-8.

Špaček, P., Sýkorová, Z., Pazdírková, J., Švancara, J. and Havíř, J.: 2006, Present-day seismicity of the south-eastern Elbe Fault System (NE Bohemian Massif). Studia Geophysica et Geodaetica, 50, No. 2, 233-258.

Steffen, H., Olesen, O., Sutinen, R. 2021b. Glacially Triggered Faulting: A Historical Overview and Recent Developments. In H. Steffen, O. Olesen, & R. Sutinen (Eds.), Glacially-triggered faulting, pp. 3-19. Cambridge University Press, 430 pp. https://doi.org/10.1017/9781108779906.

Steffen, R., Steffen, H., 2021. Reactivation of non-optimally orientated faults due to glacially induced stresses. Tectonics, 40, e2021TC006853.

Štěpančíková, P., Stemberk, J. jr., 2016. Region of the Rychlebské hory Mountains – tectonically controlled landforms and unique landscape of granite inselbergs (Sudetic Mountains). In: Pánek, T., Hradecký, J., eds., 2016. Landscapes and Landforms of the Czech Republic, Series World Geomorphological Landscapes. Springer, 263-276. https://doi.org/10.1007/978-3-319-27537-6_21.

Štěpančíková P., Fischer T., Stemberk J. jr., Nováková L., Hartvich F., Figueiredo M. P. (2019): Active tectonics in the Cheb basin: youngest documented Holocene surface faulting in central Europe? Geomorphology, 327, 472-488. https://doi.org/10.1016/j.geomorph.2018.11.007

Štěpančíková, P., Hók, J., Nývlt, D., Dohnal, J., Sýkorová, I., Stemberk, J., 2010. Active tectonics research using trenching technique on the south-eastern section of the Sudetic Marginal Fault (NE Bohemian Massif, central Europe). Tectonophysics, 485, 269-282. https://doi.org/10.1016/j.tecto.2010.01.004.

Stewart, I. S., Sauber, J. y Rose, J., 2000. Glacio-seismotectonics: ice sheets, crustal deformation and seismicity. Quaternary Science Reviews, 19, 1367-1389. https://doi.org/10.1016/S0277-3791(00)00094-9.

Stone, J.O., 2000. Air pressure and cosmogenic isotope production. Journal of Geophysical Research, 105, 23753-23759. https://doi.org/10.1029/2000JB900181.

Turpeinen, H., Hampel, A., Karow, T., Maniatis, G., 2008. Effect of ice growth and melting on the slip evolution of thrust faults. Earth and Planetary Sciences Letters 269(1):230-241. https://doi.org/10.1016/j.epsl.2008.02.017

Wells, D.L., Coppersmith, K.J., 1994. Empirical relationships among magnitude, rupture length, rupture area, and surface displacement. Bull. Seismol. Soc. Am. 82, 974–1002.

Wu, P., Steffen, R., Steffen, H., Lund, B., 2021. Glacial Isostatic Adjustment Models for Earthquake Triggering. In H. Steffen, O. Olesen, & R. Sutinen (Eds.), Glacially-triggered faulting, pp. 383-401. Cambridge University Press.

Xu, S., Freeman, S.P.H.T., Rood, D.H., Shanks, R.M., 2015. Decadal ^{10}Be, ^{26}Al and ^{36}Cl QA measurements on the SUERC accelerator mass spectrometer. Nuclear Instruments and Methods B: Beam Interactions with Materials and Atoms, 361, 39-42. https://doi.org/10.1016/j.nimb.2015.03.064.

Zweck, C., Hybrechts, P., 2005. Modeling of the northern hemisphere ice sheets during the last glacial cycle and glaciological sensitivity. J. Geophys. Res., 110, (D07103). https://doi.org/10.1029/2004JD005489.

Figure captions of all figures and tables including Supplementary material

Fig. 1. A) Site localization on the Europe map. Blue dotted line shows LGM ice sheet extent (Ehlers et al. 2011); b) Simplified tectonic map modified after Scheck et al. (2002). Main faults and fault zones: EFS – Elbe fault system zone, ISF – Intra-Sudetic main fault, LF – Lužický fault, OFS – Odra fault zone, SMF – Sudetic Marginal Fault, ZHF – Železné hory fault; Main geological units: BM – Bohemian Massif that includes also FSB and SB, FSB – Fore-Sudetic block, FSM – Fore-Sudetic Monocline, NGB – North German basin, SB – Sudetic block; c) Relief map of the Sudetes using SRTM (resolution 30m; Farr (eds.), 2007). Orange stars: epicenters of historical earthquakes with intensity (I_0) and year; Rectangles: Tertiary volcanoes; Blue dots – thermal and mineral springs; Basins: ISB – Intra-Sudetic Basin, PG – Paczków Graben, RMG – Roztoki–Mokrzeszow graben, UMG – Upper Moravia Graben, UNKG – Upper Nysa Kłodzka Graben. Mountains: GKM – Góry Kaczawskie Mts., GSM – Góry Sowie Mts., HJM – Hrubý Jeseník Mts., OHM – Orlické hory Mts., IKM – Izera – Krkonoše Mts., KSM – Kralický Sněžník Mts., RHM – Rychlebské hory Mts./Góry Złote Mts; d) current stress field from focal mechanism adopted from Špaček et al. (2006).

Fig. 2. A) Contour lines map of the trenching site. Sample positions and results of all dating methods on the isopach map of the alluvial fan deposits derived from the trenches, for results see Tab. 1.; b) Relief map of the trenching site based on LIDAR data DEM. Note the alluvial fan and its probable source valley; c) Aerial photo of the site from 2012 (source: www.mapy.cz; accessed 03 Jun 2020). 1 – reddish soil, 2 – OSL dated sediments, 3 – $IRSL_{225}$ alluvial fan deposits + geliflucted deposits + Holocene deposits, 4 – ^{10}Be dating in alluvial fan deposits, 5 – ^{14}C dated charcoals/bulk, 6 – alluvial fan deposits derived from geophysical survey, 7 – source area of the alluvial fan deposits, 8a – current channel, 8b – inferred feeder channel, 9 – trench, 10 – contour line interval 1 m, 11 – approximate offset measurements, 12 – isopach map of the alluvial fan deposits based on trenches.

Fig. 3. A) Position of the ERT profiles across the SMF and the alluvial fan on the aerial map; b) ERT profiles K-S crossing the SMF (in yellow on the map). Notice sharp borderline between Miocene clays (NE of the fault) and weathered crystalline rock (SW of the fault), with very significant resistivity

difference; c) ERT profiles DOM3 (N-S) and DOM7 (W-E), clearly showing both horizontal and vertical extent of the alluvial fan. Note: All the ERT profiles share the same resistivity scale.

Fig. 4. Log of the SE-facing wall of Trench F and the respective photomosaic. Note the non-mixed gelifluted layers. Colluvial wedges include pieces of tectonic breccia and fault gouge (black clay) from the fault zone, which gives the dark color to the deposit. For sample location from the opposite wall see Fig. S2.2.

Fig. 5. Depth profile showing results of CRN dating of fan surface.

Fig. 6. A) Predicted change in Coulomb failure stress at LGM (18 ka), relative to ice-free conditions, on a left-lateral fault plane with same orientation as SMF. Positive (negative) change in Coulomb failure stress promotes (inhibits) failure. B) Range of Coulomb failure stress change over time along the SMF (gray shading), with northern end (dashed), southern end (dotted), and Bílá Voda location (solid black line) shown. Range of stress accumulation rates during ice sheet buildup, LGM, and ice sheet retreat are indicated. Note both the highest Coulomb failure stress and the highest rate of Coulomb failure stress accumulation occur during LGM (blue shading). Ice sheet extent is adopted from Ehlers et al. (2011). Timing of latest alluvial fan deposition (tan shading) and its latest fault offset (red shading) is from this study.

Table 1. Dating results from Bílá Voda trenching site. Calibrated ages of radiocarbon dating (^{14}C) were obtained using OxCal v4.4.4 programme (after Bronk Ramsey, 2009), 2σ uncertainty and the IntCal20 atmospheric curves (Reimer et al., 2020). Optically Stimulated Luminescence (OSL) on quartz dated by GADAM Centre at Silesian University of Technology using OSL-SAR single aliquot regenerative method; CAM (Central Age Model). Infra-Red Stimulated Luminescence (IRSL) post-IR $IRSL_{225}$ dating on feldspar. For details see Supplementary material S2 – Chronology. Sample names marked in bold match the samples in trench logs in Fig. S1.1.

Italics – samples non-used due to discrepancy

* probably the age of gelifluction process not the layer accumulation, see S.2 section

■ sample of mud, but all the other samples for radiocarbon dating are charcoals

Note: e.g. trench wall NW = facing to the NW

Table 2. Parameters used in post-IR IRSL dating measurements.

Appendix A. Supplementary material:

Fig. S1.1. Geological logs of the fault-crossing trenches at the Bílá Voda site with the dated samples position. Numbers express individual lithological units, for their description see Table S1.1. For the trenches position see Fig. 2a.

Fig. S1.2. Photomosaics of selected trenches. They were produced from manually rectified photographs of individual grid fields of 0.5 x 0.5 m or 0.5 x 1.0 m size.

Fig. S2.1. a) Trench R1 log of SE-facing wall with position of radiocarbon dated samples. The dated silty layer of 9-11.2 ka calibrated ages caps the fault; b) Trench J log of SE-facing wall around the fault zone. Radiocarbon dated sample of calibrated age 42-49.7 ka recovered from colluvial wedge close to the base of alluvial fan deposits.

Fig. S2.2. a) Log of NW-facing wall of the Trench C with the position of OSL and 14C samples; b) Log of NW-facing wall of the Trench F with position of IRSL and 14C samples.

Fig. S2.3. Single grain post-IR IRSL$_{225}$ results for Bílá Voda samples from Trench F. BV15 codes represent field codes for each sample, for corresponding laboratory codes see in Table S2.1; a) single grain fading test data for sample BV15-04 measured three weeks after a dose of 21.15 Gy was administered; the red dashed line is the dose determined using a central age model, providing an estimate of 21.26 ±0.47 Gy, demonstrating no measurable fading, b) – j) single grain post-IR IRSL$_{225}$ dating results for the samples indicated in approximate stratigraphic order; data points in red = included in age calculation, open symbols = excluded; see Table S2.1 for age estimates and associated 1 sigma uncertainties; the distribution of apparent ages suggests that this gravel unit from the fan (samples BV15-02 to 11) comprises grains that were originally deposited around 100-150 ka under medium low energy conditions, and subsequently reworked between 63±6 ka and 24±4 with only very limited light exposure; grains exposed during the final depositional event are represented by the minimum age groupings highlighted in red for each sample set, with age estimates indicated by the red dashed line. Note for samples BV15-03 & 04 (plot h) collected within a single sand lens, the plot shows the combined data; this is also the case for samples BV15-06, 07, 08, and 09 (plot f).

Fig. S2.4. Comparison of Be-10 exposure ages generated from the CRONUS online calculator (wrapper version 2.2, main calculator version 2.1, constants version 2.2.1, muons version 1.1, with global production rate calibration; Balco et al. 2008) using various scaling schemes. Leftmost, constant production rate: Lal (1991)/Stone (2000) scaling scheme (black). Others, time-dependent production: red, Desilets et al. (2003, 2006); green, Dunai (2001); blue, Lifton et al. (2005); cyan, time-dependent adaptation of Lal (1991)/Stone (2000). 1 sigma internal uncertainties shown are 6%, which is the average AMS uncertainty of all the samples in the profile. The tick line – 1-sigma internal uncertainty, the thin line – 1-sigma external uncertainty.

Figure S3.1: Changes in Coulomb failure stress resolved on the SMF relative to ice free conditions for different possible model parameters: a) varying lithosphere thickness (solid colored lines) and asthenosphere relaxation time (dashed black lines) for left-lateral sense of slip at the location of the Bílá Voda trench. Thick black line represents solution shown in Figure 6. B) varying fault slip sense (colors) and range of stress changes experienced along the SMF, from north end (dashed) to south end (dotted). Stress at location of Bílá Voda indicated by solid lines.

Table S1.1. Description and interpretation of depositional environment for individual units in the trenches (see Fig. S1.1).

Table S2.1. Parameters and age estimates for post-IR $IRSL_{225}$ dating. * Combined age 06, 07, 08, 09; ** Combined age 03, 04

Table S2.2. The calculation of ^{10}Be concentration for each sample based on AMS $^{10}Be/^{9}Be$ ratios measured at SUERC and normalized to the NIST standard with assumed ratio of 2.79 x 10^{-11}.

Table S2.3. All information necessary to calculate the ^{10}Be concentrations and surface exposure age using the CRONUS online calculator (https://hess.ess.washington.edu)

Table S4.1. Parameters used in post-IR IRSL dating measurements.

Supplemental movie S3.M1 (SM1.avi)**:** modeled Coulomb failure stress from 50 – 0 relative to ice free conditions. Top panel shows map of Coulomb stress resolved onto hypothetical left-lateral fault planes oriented the same as the SMF, as in Figure 6a. Bottom panel shows Coulomb failure stress over time at the northern end of the SMF, as in Figure 6b (red line), with vertical gray line indicating the time of the current scene.

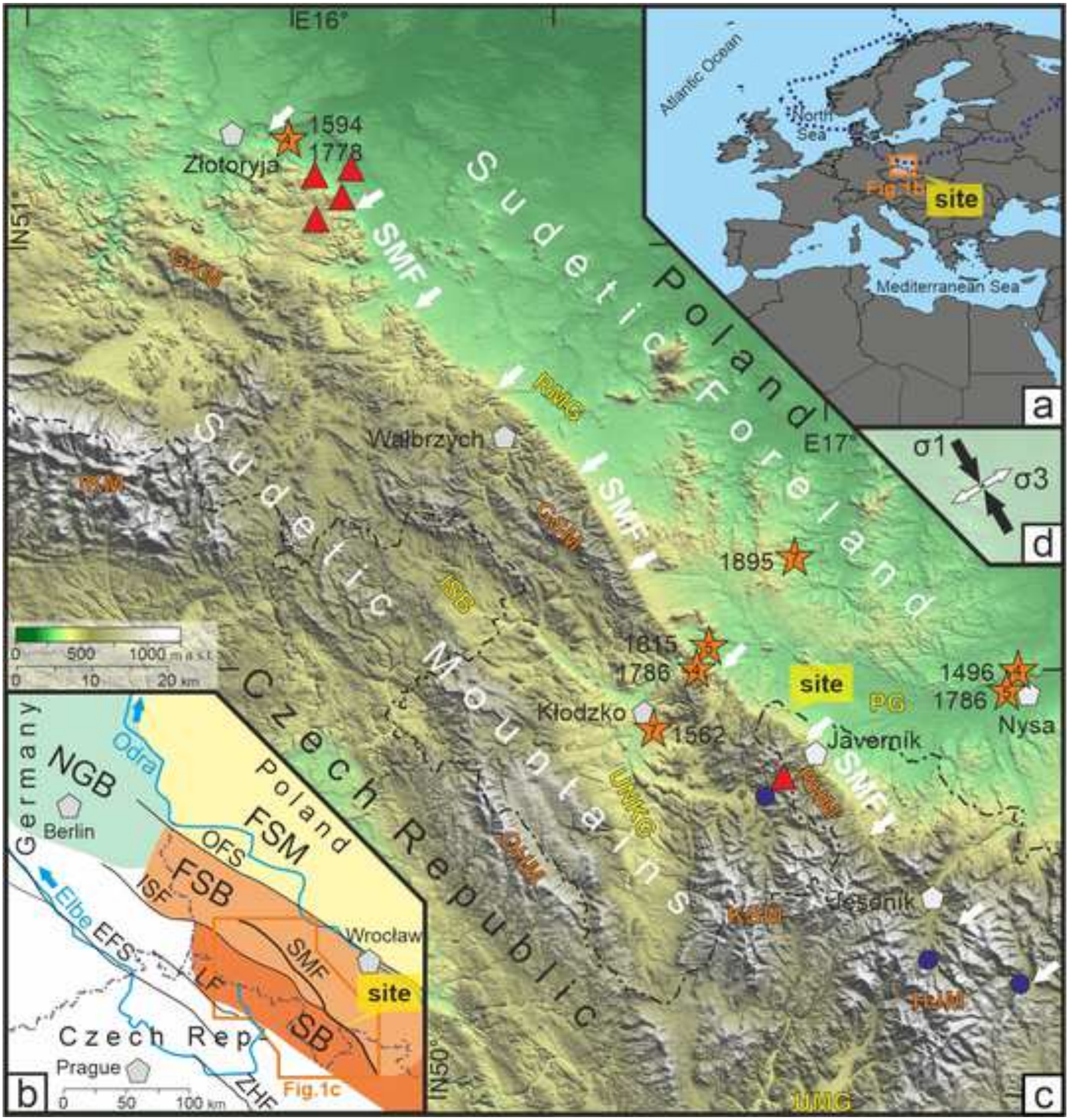
E16°
E17°
N51°
N50°
1594
1778
Złotoryja
SMF
Sudetic Foreland
Poland
Wałbrzych
Sudetic Mountains
Czech Republic
1895
1815
1786
1496
1786
site
PG
Nysa
Kłodzko
1562
Javorník
Jeseník
UMG
0 500 1000 m a.s.l.
0 10 20 km
Atlantic Ocean
North Sea
Mediterranean Sea
Fig.1c
a
σ1
σ3
d
c
Germany
Odra
NGB
Berlin
Poland
FSM
OFS
FSB
ISF
Elbe
EFS
SMF
Wrocław
LF
SB
Czech Rep.
Prague
0 50 100 km
ZHF
b

Figure 2

Click here to access/download;Figure;Fig_2.jpg

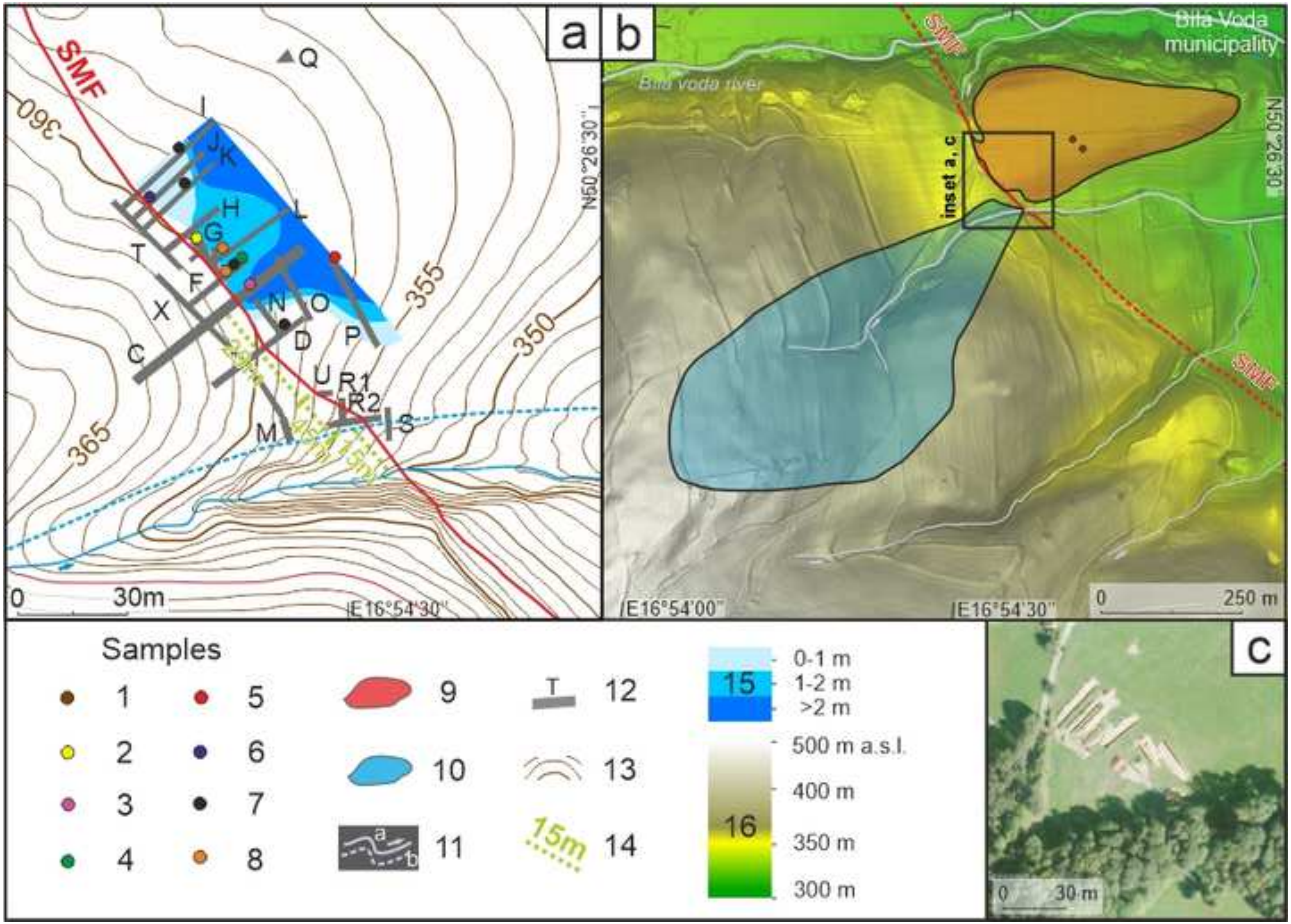

Figure 3

Click here to access/download;Figure;Fig_3.jpg

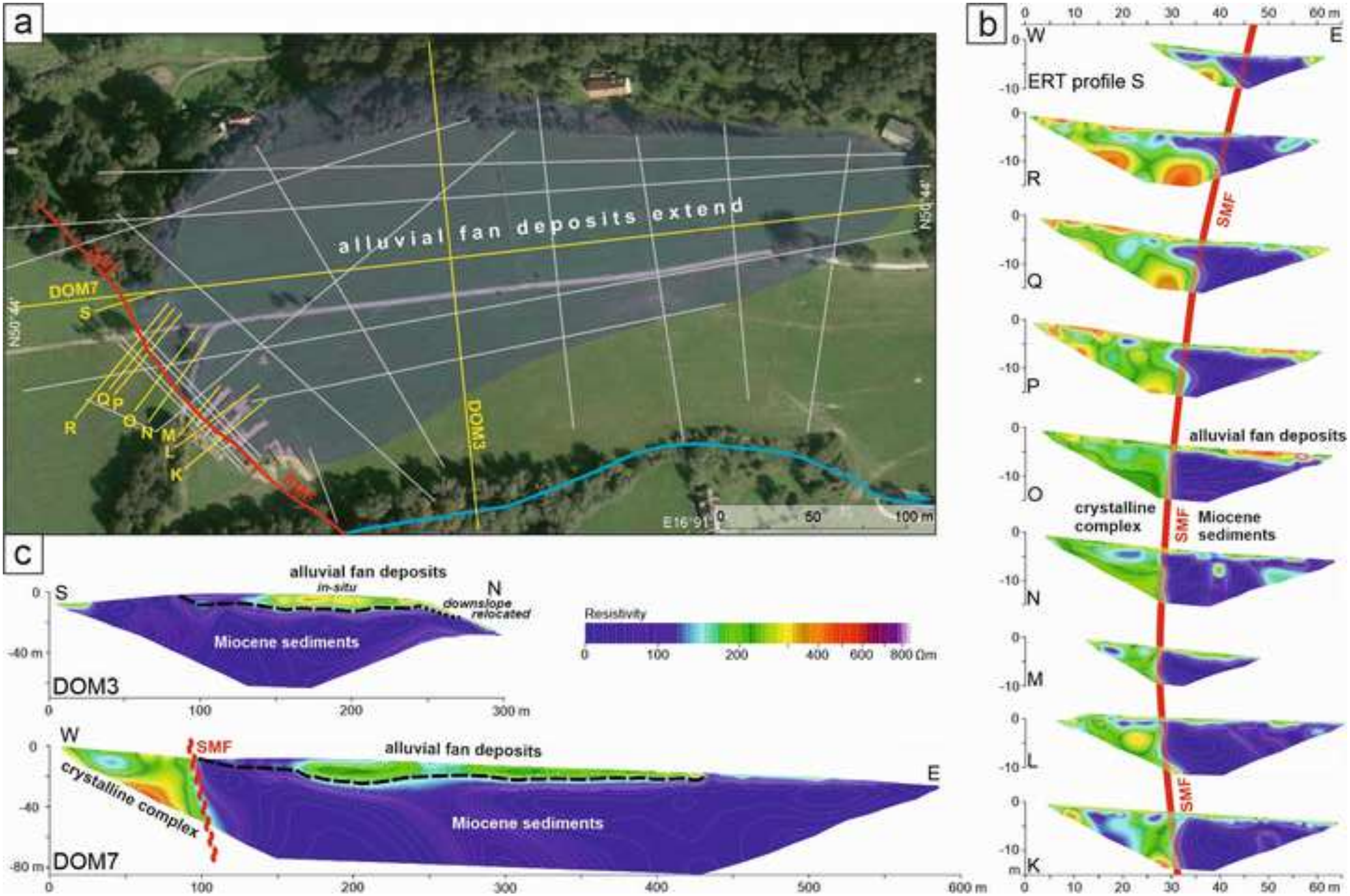

Figure 4

Click here to access/download;Figure;Fig_4.jpg

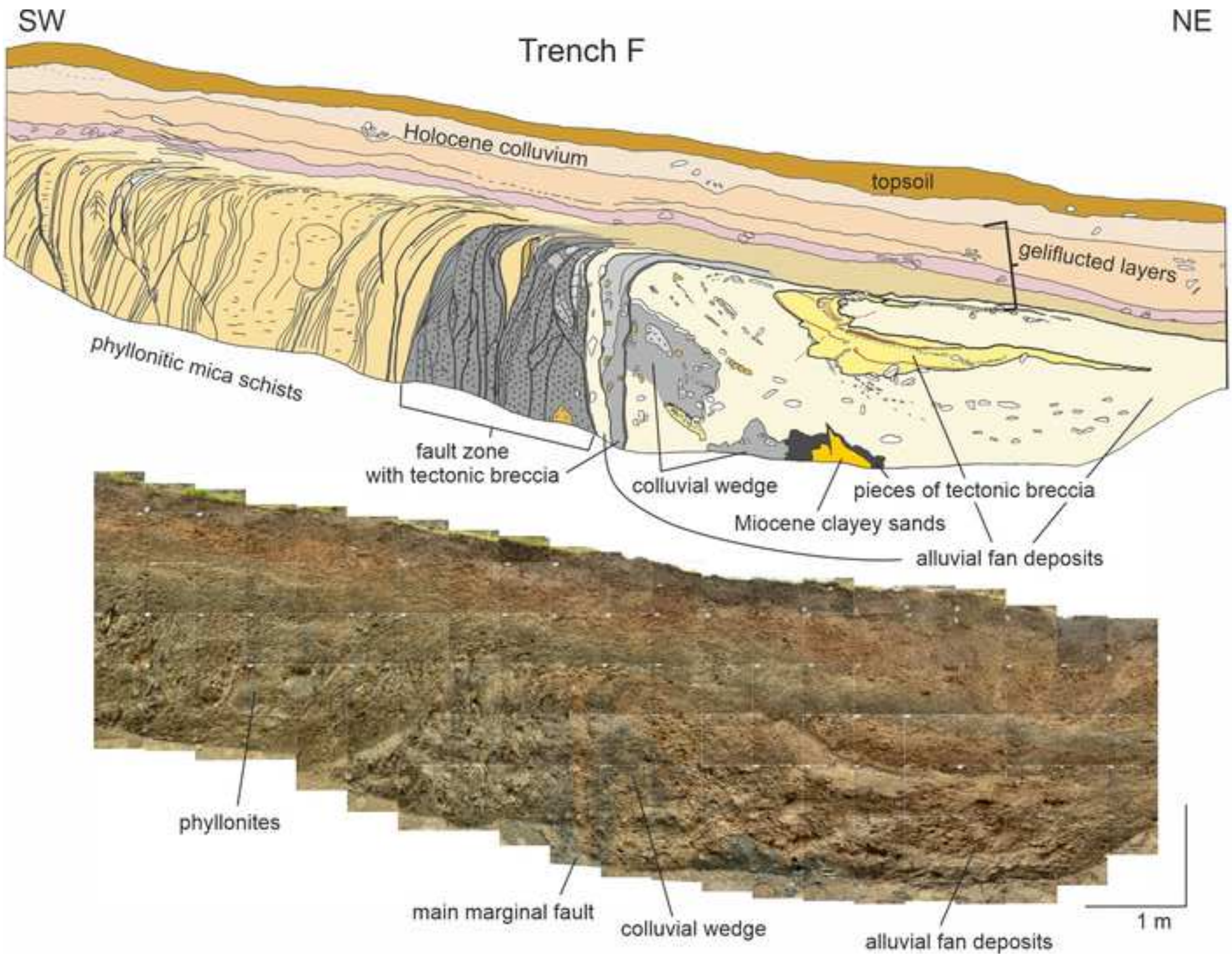

Figure 5

Click here to access/download;Figure;Fig_5.jpg

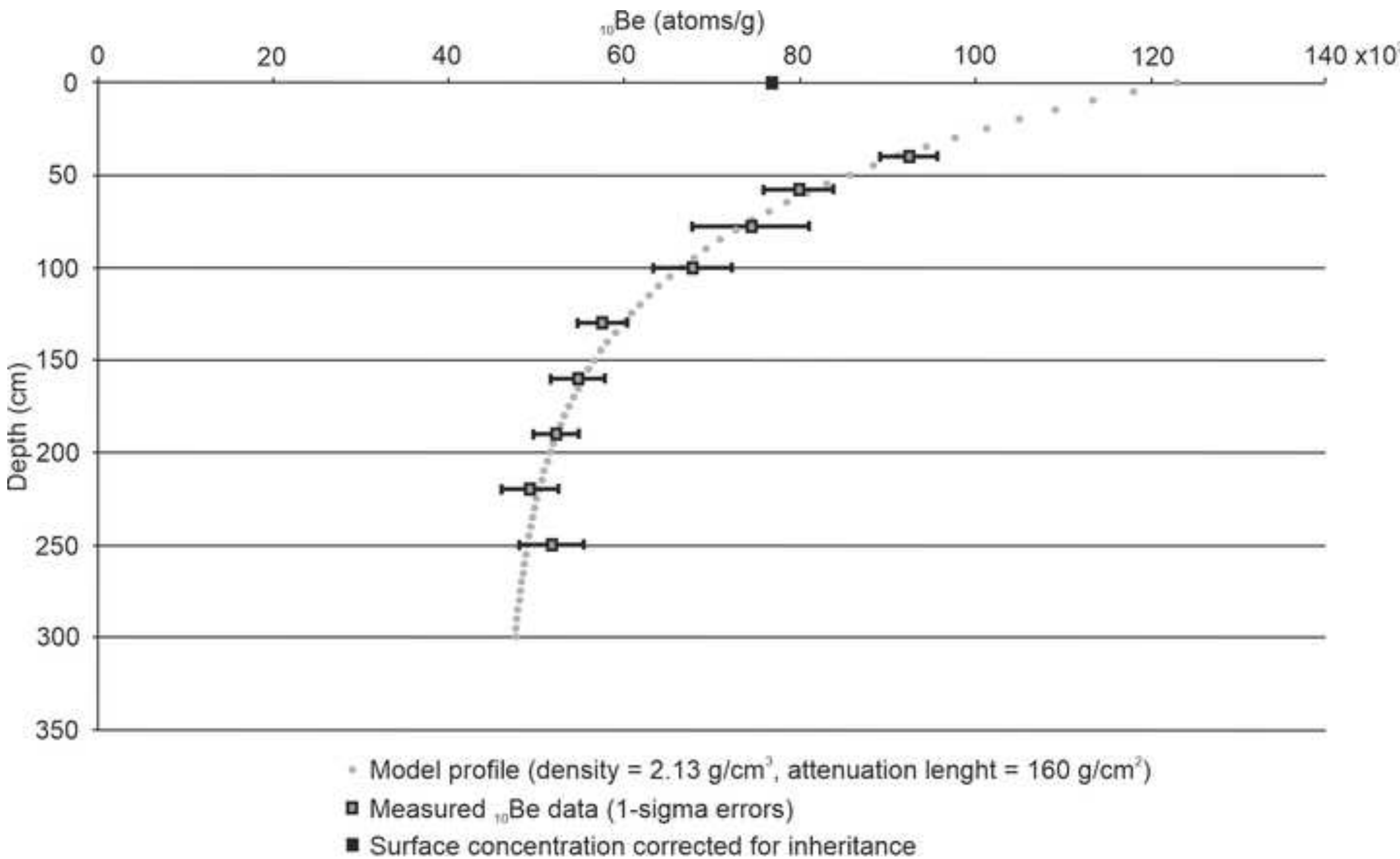

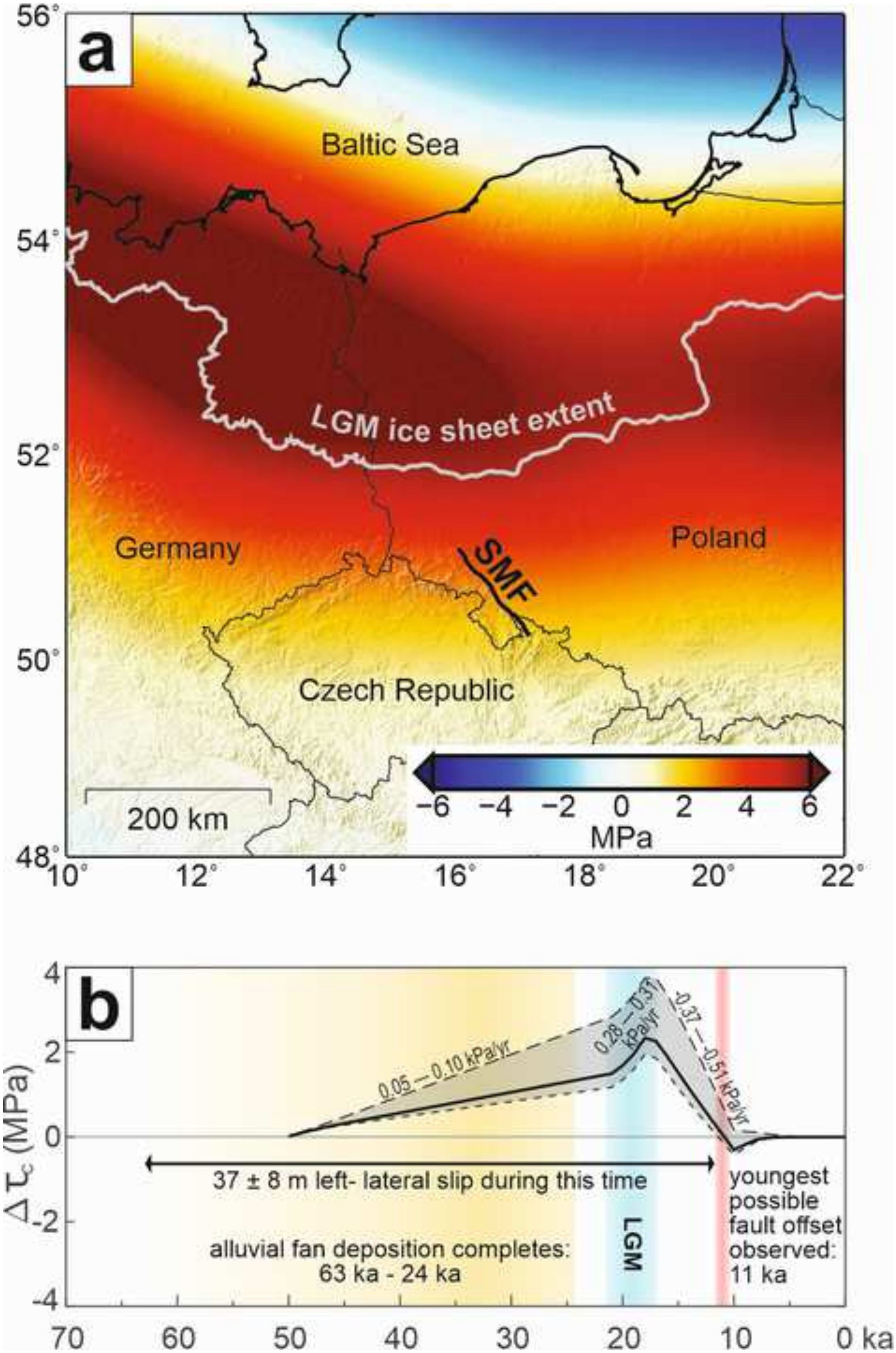
a
Baltic Sea
LGM ice sheet extent
Germany
Poland
SMF
Czech Republic
200 km
−6 −4 −2 0 2 4 6
MPa
56°
54°
52°
50°
48°
10° 12° 14° 16° 18° 20° 22°
b
0.05 – 0.10 kPa/yr
0.28 – 0.31 kPa/yr
0.37 – 0.51 kPa/yr
37 ± 8 m left- lateral slip during this time
alluvial fan deposition completes:
63 ka - 24 ka
LGM
youngest
possible
fault offset
observed:
11 ka
Δτc (MPa)
4
2
0
-2
-4
70 60 50 40 30 20 10 0 ka

Stratigraphy Unit/Material	Dating method	Sample names	Trench wall facing to	Uncalibrated ^{14}C ages (BP)	Calibrated ^{14}C age (cal. yr. BP) or luminescence age	Comment
50-60 Holocene colluvium/polymict material	^{14}C	**Ti 18**	TI SE	375 ± 20	325-498	
		Ti 16	TI SE	790 ± 15	680-726	
		Bila Voda **F 50**	TC NW	845 ± 30	684-791	
		Bila Voda **F 13**, C 11	TF SE	1180 ± 90	932-1282	
		Bila Voda **DJV 4**	TD SE	1190 ± 20	1061-1178	
		Bila Voda **FJV 16**	TF SE	2130 ± 25	2002-2293	
		Bila Voda **DSZ 7**	TD NW	3200 ± 40	3349-3487	
	$IRSL_{225}$	BV15-**13**	TF NW		0.77 ± 0.12 ka	
	^{14}C	BV **Ti 1**	TI SE	3980 ± 15	4413-4518	
		BV **Ti 5**	TI SE	4070 ± 25	4441-4796	
		Ti 3	TI SE	4535 ± 25	5051-5314	
		BV Tk 1	TK SE	2100 ± 15	2001-2116	
fluvial to colluvial layer in recent valley/silty layers	^{14}C	TR 2 1	TR2 W	8200 ± 20	9026-9275	fault sealing layers (TR 2 1, TR 1 V, TR 1 VII, TR 1 VIII)
		TR 1 V	TR1 SE	9660 ± 25	10812-11190	
		TR 1 VII	TR1 SE	9595 ± 20	10771-11133	
		TR 1 VIII	TR1 SE	9685 ± 20	10889-11197	
100-140 - geliflucted, solifluted layers/monomict material	^{14}C	*BV **Ti 20***	*TI SE*	*1935 ± 15*	*1821-1926*	
		Ti 8	*TI SE*	*1865 ± 15*	*1723-1824*	
		*Bila Voda **F 18**, E19*	*TF NW*	*1200 ± 60*	*973-1273*	burnt root
		*Bila Voda **F 19**, E20*	*TF NW*	*1080 ± 170*	*690-1295*	burnt root
		*Bila Voda **D 12**, F25*	*TD NW*	*1120 ± 90*	*801-1272*	bioturbation, charcoal in a fault fissure
		*Bila Voda **D1**/0.75m*	*TD SE*	*2510 ± 30*	*2490-2735*	burnt root
	$IRSL_{225}$	BV15-**12**	TF NW		30.6 ± 4.2 ka	
150 – alluvial fan/gravels, sometimes with silty layers	^{10}Be	SMF-P1	TP SW		~13.1 ka *	best fit, most probably represents age of gelifluction
	$IRSL_{225}$	BV15-**11**	TF NW		24.1 ± 3.7 ka	
		BV15-**10**	TF NW		30.8 ± 4.1 ka	
160 – alluvial fan deposits/silty layer	^{14}C	*BV L-**F6**/RES* ■	*TL NW*	*4725 ± 40*	*5323-5581*	? translocation of Holocene organic acids (BV L-F6/RES, BV L-F6/NaOHsol, BV F F31/1.5m)
		*BV L-**F6**/NaOHsol* ■	*TL NW*	*5660 ± 30*	*6318-6530*	
		*BV F **F31**/1.5m* ■	*TF SE*	*7200 ± 30*	*7938-8159*	
	OSL	*Bila Voda 5 (J63) **BV5***	*TC SE*		*2.6 ± 1.2ka*	
		Bila Voda 4 (J60) **BV4**	TC NW		20.1 ± 5.5ka	
	$IRSL_{225}$	BV15-**09**	TF NW		53.2 ± 3.0 ka	combined age 06, 07, 08, 09
		BV15-**08**	TF NW		53.2 ± 3.0 ka	
		BV15-**07**	TF NW		53.2 ± 3.0 ka	
		BV15-**06**	TF NW		53.2 ± 3.0 ka	
170 – alluvial fan deposits/gravels	$IRSL_{225}$	BV15-**05**	TF NW		37.1 ± 3.1 ka	
175 – alluvial fan deposits/silty-sandy layer	OSL	Bila Voda 3 (K58) **BV3**	TC NW		23.2 ± 1.3ka	
190 – alluvial fan deposits/silty layer	^{14}C	*BV F **H18**/2.5m* ■	*TF NW*	*5650 ± 25*	*6320-6494*	? translocation of Holocene organic acids
	$IRSL_{225}$	BV15-**04**	TF NW		54.6 ± 5.8 ka	combined age 03, 04
		BV15-**03**	TF NW		54.6 ± 5.8 ka	
203 – colluvial wedge/silty-sandy layer	^{14}C	BV **Tj 1**	TJ SE	40900 ± 2500	41772-54395	the larger uncertainties are due to the small sample size
215 – within colluvial wedge/silty-sandy layer	OSL	Bila Voda 2 (L56) **BV2**	TC NW		26.5 ± 1.3 ka	
	$IRSL_{225}$	*BV15-**01***	*TF SE*		*14.1 ± 2.4 ka*	
210 – base of alluvial fan/gravels	$IRSL_{225}$	BV15-**02**	TF NW		62.9 ± 6.1 ka	
vertically dragged layer in fault zone /silty layer		Bila Voda G1 **BVG1**	TG		56.4 ± 2.6ka	trench bottom sampled, position showed at TL
		Bila Voda G2 **BVG2**	TG		76.6 ± 6.6ka	

CRediT author statement.

Since the research was multidisciplinary, the authors had multiple roles within their own discipline contribution.

Petra Štěpančíková: Conceptualization, Methodology, Validation, Formal analysis, Investigation, Data curation, Writing – Review and Editing, Visualization, Supervision, Project administration, Funding acquisition; **Thomas K. Rockwell**: Conceptualization, Methodology, Validation, Formal analysis, Investigation, Writing – Original Draft preparation, Review and Editing, Supervision; **Jakub Stemberk:** Investigation, Visualization; **Filip Hartvich**: Methodology, Validation, Formal analysis, Investigation, Visualization; **Edward J. Rhodes**: Conceptualization, Methodology, Software, Validation, Formal analysis, Investigation, Writing – part of Original Draft, Review and Editing, Visualization; **Madeline Myers**: Validation, Formal analysis, Investigation, Data Curation, Writing – part of Original Draft; **Karen Luttrell**: Conceptualization, Methodology, Software, Validation, Formal analysis, Investigation, Writing – part of Original Draft, Review and Editing, Visualization, Supervision; **Petr Tábořík**: Methodology, Formal analysis, Investigation, Writing – Original Draft, Visualization; **Dylan H. Rood**: Methodology, Validation, Formal analysis, Investigation, Writing – Original Draft, Visualization; **Neta Wechsler**: Investigation, Writing – Original Draft; **Daniel Nývlt**: Investigation, Writing – part of Original Draft, Review and Editing; **María Ortuño**: Investigation, Writing – Review and Editing; **Jozef Hók**: Investigation